



## Advanced calibration of a 3D masonry arch bridge model using non-destructive testing and numerical optimisation

B. Pantò<sup>a,b,\*</sup>, J. Ortega<sup>c,d</sup>, S. Grosman<sup>b</sup>, D.V. Oliveira<sup>d</sup>, P.B. Lourenço<sup>d</sup>, L. Macorini<sup>b</sup>, B. A. Izzuddin<sup>b</sup>

<sup>a</sup> Department of Engineering, Durham University, Durham, UK

<sup>b</sup> Department of Civil and Environmental Engineering, Imperial College London South Kensington Campus, London SW7 2AZ, United Kingdom

<sup>c</sup> Institute for Physical and Information Technologies (ITEFI) Leonardo Torres Quevedo, Consejo Superior de Investigaciones Científicas (CSIC), C/Serrano 144, Madrid 28006, Spain

<sup>d</sup> Institute for Sustainability and Innovation in Structural Engineering (ISISE), University of Minho, Azurém Campus, Guimarães, Portugal

### ARTICLE INFO

#### Keywords:

Historic bridges  
Cultural heritage  
In-situ tests  
Non-destructive testing techniques  
FEM models  
Macroscale models  
Model updating  
Metamodels  
Bayesian methods  
Genetic algorithms

### ABSTRACT

Historical masonry arch bridges constitute the backbone of many existing transportation networks in different countries in Europe and worldwide. They represent valuable cultural heritage assets and play an essential social and economic role. Since construction, old masonry bridges have accumulated structural damage from traffic and environmental actions. Furthermore, depending on their geometrical and mechanical characteristics, they may be particularly vulnerable to extreme events like earthquakes. Thus, accurate structural assessment under different loading conditions is critical for the conservation of these structures. Realistic assessment requires suitable numerical models to represent the characteristic 3D behaviour. The complexity of this task is further compounded by the practical difficulty in obtaining essential information on the internal bridge structure and the masonry mechanical parameters, which are vital to achieve accurate response predictions against service and extreme actions.

This paper presents an advanced calibration procedure for a refined macroscale bridge model, allowing for the anisotropic nature of the masonry material. The proposed calibration approach is applied to an actual multi-span masonry viaduct, where sonic, ultrasonic, and ground penetrating radar tests are conducted to investigate the internal structure of the viaduct and determine the elastic properties of the masonry materials. In addition, the dynamic characteristics of the bridge are evaluated through in-situ measurements under environmental vibrations and used for model validation. The results from a standard simplified model calibration and an enhanced calibration are compared considering the vibration modes of the bridge. Simplified calibration is carried out using the results from in-situ tests, while a statistic inference procedure and numerical optimisation are adopted in the refined calibration to achieve improved accuracy. Although the paper focuses on a specific case study, the adopted methodology can be easily applied to studying other masonry bridges and cultural heritage masonry structures.

### 1. Introduction

Masonry arch bridges represent vital transportation infrastructures for many countries worldwide. In Europe, about 200,000 masonry railway bridges are still in service. They constitute approximately 60% of the existing bridge stock [1], playing a crucial role in the economic and social life of the countries where they are located. However, most masonry bridges are more than one hundred years old and have been

subjected to increasing traffic loading [2] and extreme environmental actions, as the effects of earthquakes or foundation scouring [3,4] due to river flooding, leading to progressive accumulation of damage that in turn can cause the reduction of structural performance or even bridge collapse [5,6]. Accurate simulation of the bridge response under different loading conditions, accounting for a realistic description of the different bridge components and their interaction, is essential to assess structural safety and implement potential strengthening to preserve and

\* Corresponding author at: Department of Engineering, Durham University, Durham, UK.

E-mail address: [bartolomeo.panto@durham.ac.uk](mailto:bartolomeo.panto@durham.ac.uk) (B. Pantò).

<sup>1</sup> Orcid: 0000-0002-3340-228X

<https://doi.org/10.1016/j.conbuildmat.2024.137131>

Received 12 February 2024; Received in revised form 25 May 2024; Accepted 15 June 2024

Available online 1 July 2024

0950-0618/© 2024 The Author(s). Published by Elsevier Ltd. This is an open access article under the CC BY license (<http://creativecommons.org/licenses/by/4.0/>).

maintain such valuable cultural heritage assets. In this regard, advanced assessment frameworks have been recently proposed and applied to determine the ultimate load-carrying capacity of masonry arch bridges, accounting for material and geometric uncertainties and statistical descriptions of traffic and environmental actions [7,8].

Typical 2D modelling strategies for evaluating the load capacity of masonry bridges are based on limit analysis methods, which require a limited number of model parameters to obtain results that are easy to interpret [7,9]. However, more sophisticated models are needed to account for the complex 3D response and local failure mechanisms such as the out-of-plane failure of spandrel walls, ring separation in multi-ring arch bridges, and the actual nonlinear interaction between backfill and the masonry parts of the bridge [10]. Macroscale [11] or mesoscale [4] finite element models or discrete modelling approaches [12–14] can properly simulate crack propagation in the masonry and masonry-backfill separation and sliding. However, these refined approaches require complex 3D plastic damage constitutive laws and sophisticated calibration procedures [10,15] to determine several model material parameters.

The in-situ mechanical characterisation of masonry arch bridge materials (masonry, backing and backfill) and the evaluation of the bridge internal structure are complex tasks, bringing practical difficulties due to the characteristic structural complexity and the inaccessibility to some portions of the structure. In addition, masonry bridges represent valuable cultural heritage, often protected by law.

Minor destructive tests such as flat-jack tests or endoscopies are consolidated methods, but their application is typically limited to avoid causing extensive damage to the protected material fabric. Moreover, flat-jack tests cannot be used to characterise the inner core filling material and are highly time-consuming.

For this reason, non-destructive tests (NDTs) have attracted the interest of the academic and engineering communities. Many techniques, including sonic methods, Ground Penetrating Radar (GPR) tests, and infrared thermography, have been validated against the results of more invasive tests [16,17] and then used to study masonry bridge components [6,18]. However, fewer attempts to characterise the backfill material through geophysics tests have been performed in the literature. One example is represented by [19], where multi-sources of non-destructive methods have been employed, including terrestrial laser scanner and GPR tests to determine the bridge external and internal geometry, and multichannel analysis of surface waves (MASW) for characterising the backfill.

The accuracy of the information provided by NDTs and the consequent model calibration can be effectively validated or improved by performing ambient vibration measurements, which offer an experimental evaluation of the fundamental modes of vibration of the bridge, including frequencies and mode shapes. The experimental dynamic properties can be compared with those provided by the calibrated numerical model [19], or used within advanced model updating procedures to improve the accuracy of the parameters evaluated by NDTs or establish unknown parameters not experimentally assessed [20].

This paper presents the results of an extensive in-situ experimental campaign conducted on a 5-span railway viaduct in Northern Portugal. The study aims to achieve a detailed geometrical characterisation of the bridge and the elastic masonry properties for a refined 3D macroscale bridge model [11] by combining different non-destructive material tests and environmental vibration measurements. According to the adopted strategy, the optimal mechanical parameters of masonry and infill materials are determined by solving a multi-modal optimisation problem based on statistic inference and metaheuristic models to limit the computational effort due to the dimension of the problem and the number of unknown parameters. The results confirm that NDTs can be effectively used to achieve a detailed characterisation of the bridge structure when combined with the proposed refined model calibration procedure. Despite focusing on a specific case study, the presented methodology is general and can be easily applied to other existing

masonry structures.

## 2. The case study

The paper investigates the *Quebradas* viaduct (Fig. 1a) belonging to the *Linha do Douro* railway line, Baião, northern Portugal. It is a 5-span bridge, characterised by relatively large spans of 20 m, tall piers with variable height from 18 m to 29 m and large transversal slenderness due to a narrow cross-section of approximately 5 m width (Fig. 1b). These geometric features render the bridge vulnerable to transversal lateral loads, such as the inertia forces induced by earthquakes. The masonry viaduct was built in the 1930s to replace a steel bridge structure. The Portuguese infrastructure company provided detailed technical documentation for the original masonry bridge project, as schematically displayed in Fig. 2.

The external layers of the piers, barrel vaults and spandrel walls are made of granitic stone masonry with 600 mm × 300 mm (length × height) blocks connected by 10 mm thick mortar joints (Fig. 3). The core of the piers is filled with concrete material (Fig. 2) as specified in [21] and confirmed by the in-situ tests. Fig. 4 displays a longitudinal view (Fig. 4a) and a vertical section (Fig. 4b) highlighting critical external and internal features of the masonry viaduct. Importantly, two different geometrical layouts of the barrel vaults can be observed, in which a constant-thickness arch characterises the two end faces below the spandrel walls (Fig. 4a). In contrast, the internal arch has a variable thickness, as displayed in Fig. 4b, where the horizontal dashed lines indicate changes in the thickness of the spandrel walls. From the technical documentation, it can be seen that the concrete backing layer extends approximately up the vital section of the arches. According to historical information [21], a backfill layer of soil or masonry materials is located above the backing. In previous research [7], the ultimate load-carrying capacity of the bridge was evaluated using 2D limit analysis procedures, also considering geometric and mechanical uncertainties within a probabilistic framework. The technical drawings indicate that the piers are supported by sturdy foundations constructed on firm soil (see Fig. 2b), allowing the piers to be considered fully fixed at their base.

## 3. In-situ tests

### 3.1. Dynamic identification

The dynamic properties of the viaduct were evaluated by applying an output-only modal identification procedure. This technique is widely applied in the context of historical structures, where the dynamic



Fig. 1. Quebradas viaduct: (a) global view of the bridge and (b) detail of the railway track.



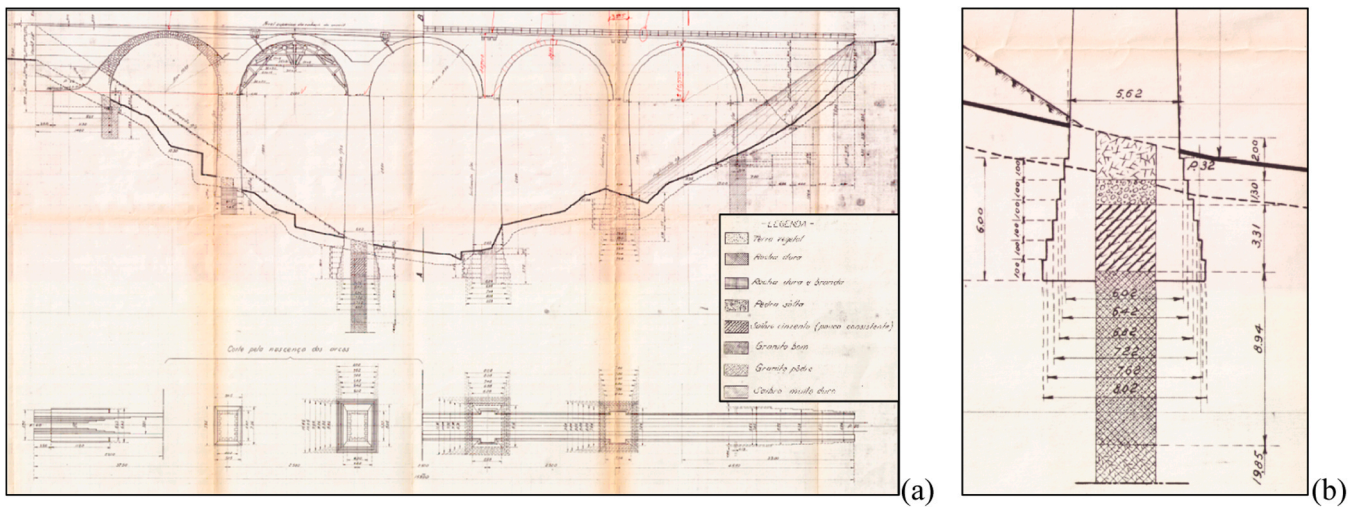


Fig. 2. Original drawing provided by Portuguese infrastructure company; a) longitudinal section; b) detail of a pier foundation structure and soil.

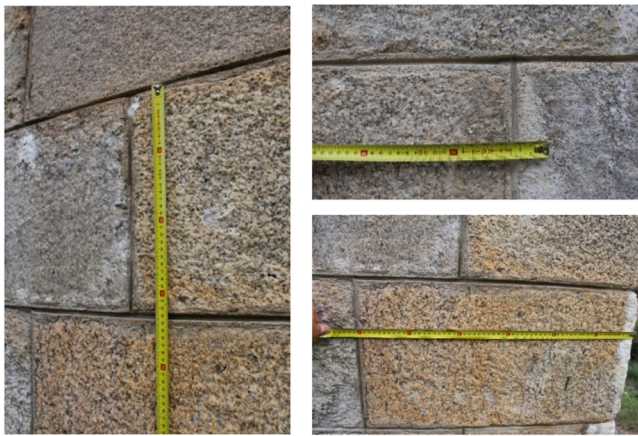


Fig. 3. Masonry details at the base of the first pier from the northern side of the viaduct.

response is measured using ambient excitations, as those caused by wind and traffic, which are random in time and space. The procedure requires the installation of accelerometers on the bridge at different locations to record the accelerations of the structure (Fig. 5). The used equipment included uniaxial piezoelectric accelerometers (PCB model 393B12) with a sensitivity of 10 V/g and a frequency range from 0.15 to 1000 Hz (measurement range  $\pm 0.5$  g), a data acquisition system from National Instruments (cDAQ-9174 chassis and three 4-channel modules NI-9234), a personal computer and cables, Fig. 5.

Tests were carried out with accelerometers located at the top of the spandrel walls, in correspondence with the middle section of piers and half-span sections. The sensor layout showing the location and direction of the accelerometers is schematically illustrated in Fig. 6. Here, the two accelerometers marked in blue at the middle of the central span, where the largest displacements are expected to occur, were used as reference accelerometers to correlate the two setups carried out. Since the two sides of the bridge are expected to behave uniformly, most of the accelerometers were placed on the same side of the viaduct. Only three accelerometers were placed on the other side to corroborate the assumed uniform behaviour. Based on the expected fundamental mode shape, most accelerometers were arranged horizontally, perpendicularly to the bridge longitudinal direction (direction Y in Fig. 6). Two pairs of vertical accelerometers were placed at two positions along the longitudinal axis of the viaduct on both sides to capture possible rotations of the top

structure of the bridge due to the flexural deformation of the piers. The frequency sampling used during the recording was equal to 200 Hz. The total recording duration for each test setup varied between 20 and 30 minutes.

The results were processed by ARTEMIS software [22]. Three methods were used for the modal identification: (a) Frequency Decomposition Domain (FDD), (b) Enhanced Frequency Decomposition Domain (EFDD) and (c) Stochastic Subspace Identification based on Unweighted Principal Component (SSI-UPC). Fig. 7 shows the results of the EFDD and SSI analyses. The combination of the three methods allowed the identification of the first four natural modes of the bridge with associated frequencies, reported in Table 1.

The consistency of the modes obtained by the EFDD and the SSI-UPC methods was evaluated using the Modal Assurance Criterion (MAC), a statistical indicator ranging from 0 to 1, with 1 indicating complete consistency [23,24]. The results are presented in Table 2. All MAC values are higher than 0.8, confirming that the modes are substantially independent from the adopted approach (usually, values close to 0.9 indicate a consistent correspondence of the two mode shapes).

The four natural mode shapes identified are shown in Fig. 8. As expected for this structural typology, the first three modes involve transversal horizontal movement of the bridge. Mode 1, with a frequency of about 1.66 Hz, is the fundamental mode of the structure with no inflexion point. Mode 2 and mode 3, with frequencies of about 2.69 Hz and 3.95 Hz, are other transversal modes with one and two inflexion points, respectively. Finally, Mode 4, with the frequency of 5.23 Hz, is the first vertical mode of the structure, which is mainly captured by the vertical accelerometer at the middle of the central span.

The measured modes describe the typical structural behaviour of a long viaduct with multiple piers whose longitudinal dimension is significantly larger than the width. Several piers along the viaduct length inhibit the development of local vertical modes for the individual barrel vaults. The bridge also shows an overall nearly symmetrical behaviour, despite some height differences for the northern and southern piers. The second and third modes show slightly higher amplitudes in the north side, which may indicate higher structural flexibility at that side of the bridge.

### 3.2. Sonic and ultrasonic tests

Acoustic sonic and ultrasonic tests were carried out on the viaduct piers. These tests, which are widely used for structural diagnosis of historical masonry structures [25-27], are based on evaluating the characteristics of the propagation of elastic waves within the

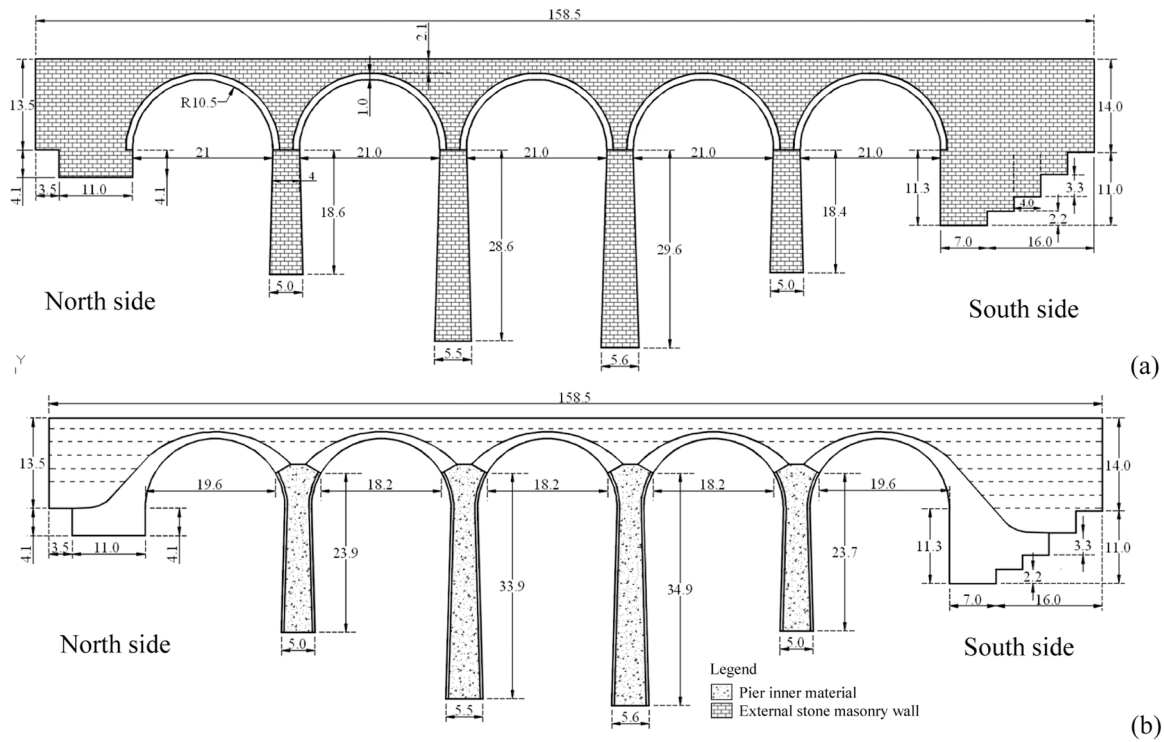


Fig. 4. Geometrical characteristics of (a) the external and (b) internal structure of the viaduct (dimensions in m).

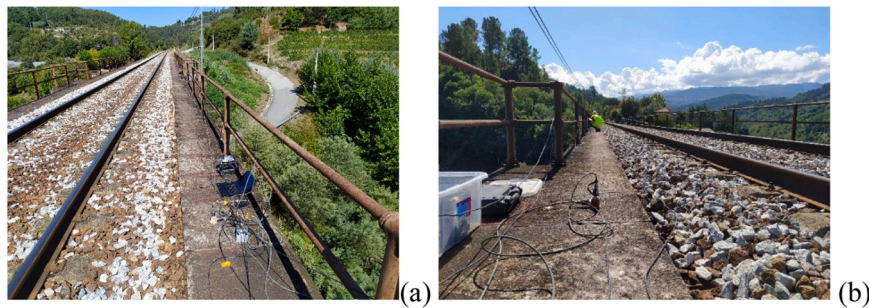


Fig. 5. Dynamic identification tests: (a) view of the data acquisition system, computer, and accelerometers, located at the top of the bridge; and (b) accelerometers placed along the top of the bridge.

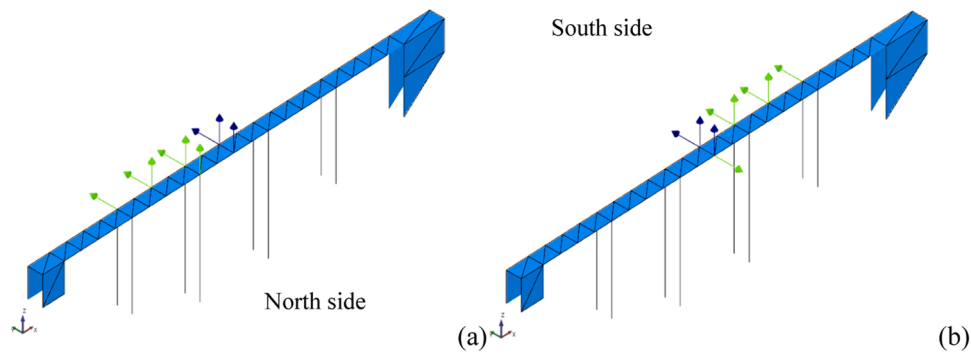


Fig. 6. Schematic location of the accelerometers in the dynamic identification test at the top of the viaduct (the positive x direction corresponds approximately to the south): (a) test setup 1; (b) test setup 2.

investigated structural component. The wave propagation velocity is measured, allowing the evaluation of the physical and mechanical properties of the structural material, namely Poisson's ratio and dynamic modulus of elasticity [25]. Sonic tests were executed utilising an

impact hammer (PCB model 086D05) with a measurement range of  $\pm 22,240$  N pk, one accelerometer (PCB model 352B) with a measurement range of  $\pm 5$  g and 1000 mV/g sensitivity, a personal computer, cables and a data acquisition system from National Instruments



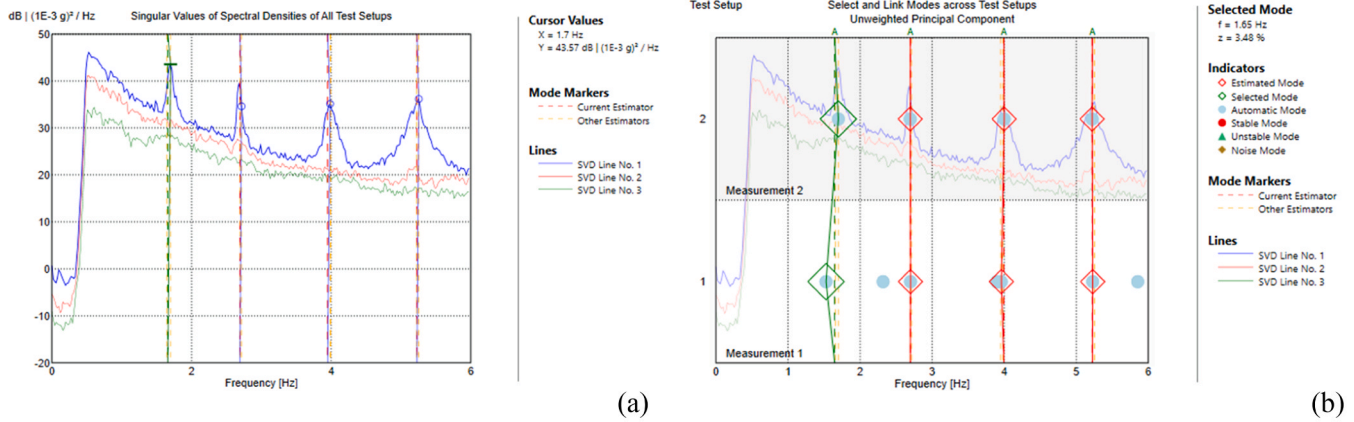


Fig. 7. Mode selection using different methods: (a) EFDD; (b) SSI-UPC [22].

**Table 1**  
Natural frequencies of the first four modes by FDD, EFDD and SSI-UPC methods.

Modes	Frequencies (Hz)		
	FDD method	EFDD method	SSI-UPC method
Mode 1	1.70	1.66	1.62
Mode 2	2.72	2.69	2.70
Mode 3	3.98	3.95	4.00
Mode 4	5.25	5.23	5.22

**Table 2**  
MAC values comparison between the EFDD and the SSI-UPC mode shape results.

Mode 1 (1.623 Hz)	Mode 2 (2.697 Hz)	Mode 3 (3.995 Hz)	Mode 4 (5.223 Hz)
0.84	0.92	0.99	0.84

(cDAQ-9174 chassis and one 4-channel module NI-9234). The ultrasonic tests were conducted using Pundit Lab equipment with 0.1 μs precision and 54 Hz frequency transmission transducers.

The tests were performed at the base of the first pier from the southern side of the bridge. A multi-step procedure was used to characterise the stone material properties, the thickness of the external walls and the properties of the inner core of the pier. It consists of 4 steps:

- (1) Ultrasonic tests on the stone blocks (US). These tests aim to obtain the wave propagation velocity within the stone blocks of the external layer of the pier.
- (2) Impact-echo tests on the stone blocks (IE). After estimating the wave propagation velocity within the stone blocks, the impact echo technique is employed to assess the thickness of the stone masonry layer.
- (3) Direct sonic tests on the stone masonry pier (DS). After knowing the wave propagation velocity within the stone blocks and the

thickness of the stone masonry layer, direct sonic tests allow for the estimation of the velocity throughout the core of the pier.

- (4) Indirect sonic tests on the stone masonry pier (IS). Indirect sonic tests contribute to evaluating the elastic properties of the stone masonry external layer of the piers.

More in detail, the characterisation of the pier materials was carried out by five ultrasonic tests (US-1,, US-5), five impact echo tests (IE1,, IE5), four direct sonic tests (DSA, DSB, DSC1, DSC2), and twenty indirect sonic tests performed using two 3×3 grids (grid A and grid B on the pier transversal southern and northern side), denominated IS-A1,, IS-A9, and IS-B1,, IS-B9. The specific locations of the tests are shown in Fig. 9.

### 3.2.1. Ultrasonic tests on stone blocks

Ultrasonic tests on stone blocks were performed using the indirect transmission method by placing both transducers on the external surface of the blocks, as the internal surface was inaccessible. The wave propagation velocity is computed by dividing the distance between transducers into the time of flight, i.e., the time it takes for the ultrasonic wave to propagate from the transmitter to the receiving transducer. Indirect sonic tests provide both primary (P) wave velocity ( $v_p$ ) and surface or Rayleigh (R) wave velocity ( $v_R$ ). Two examples of the common waveforms obtained from an indirect test are shown in Fig. 10. The first waves arriving are the P waves, which have greater velocity but lower amplitude. The increase in the amplitude of the waveform typically corresponds to the R waves, which are stronger [25]. In Fig. 10, the arrival of the P wave is indicated at point “1” and the arrival of the R wave at point “2”.

It should be noted that a perfect coupling between the transducer and the stone surface was not fully achieved, thus the signal received was low (particularly when increasing the distance between the transducers). This rendered the identification of the exact point of arrival of the P-wave with lower energy and amplitude particularly difficult. As a result, the analysis focused on identifying the arrival of the R-waves, which was clearer for all signals.

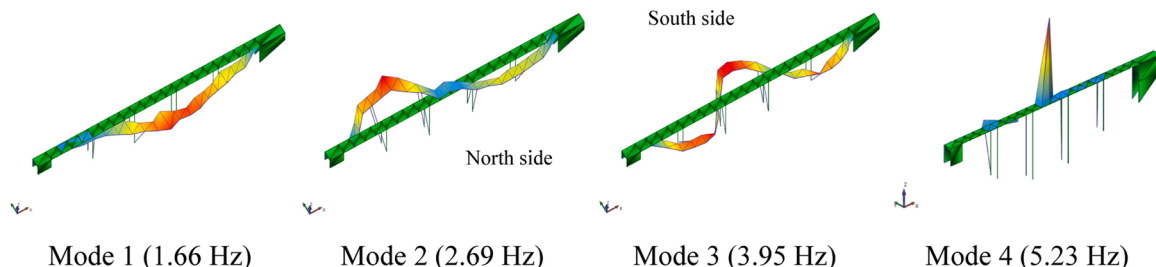


Fig. 8. Mode shapes of the first four natural modes obtained by the EFDD method.

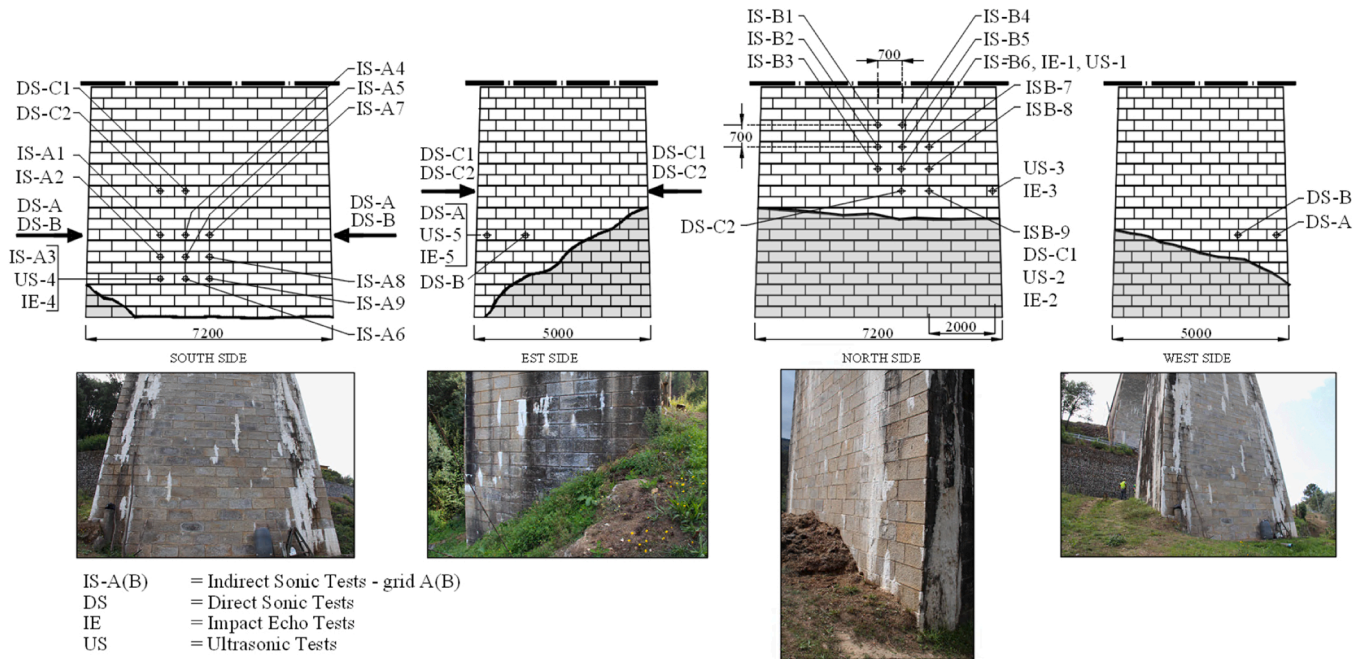


Fig. 9. Sonic and ultrasonic tests conducted at the base of the first pier from the bridge's southern side.

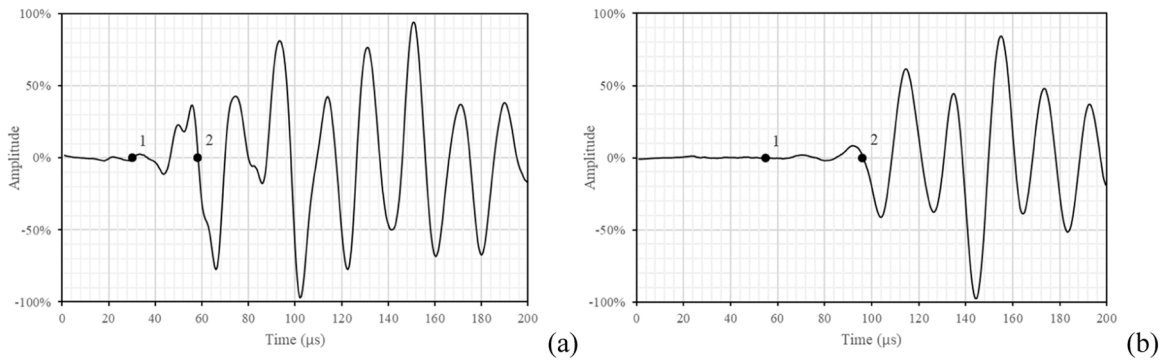


Fig. 10. Example of waveforms received and characteristic points of arrival of P waves (1) and R waves (2). Note that the vertical axes are normalised by the maximum amplitude measured; a) sample US-5 ( $d = 100$  mm) and b) sample US-4 ( $d = 200$  mm).

Following the recommendations from the European Standard [28], the wave velocity can be evaluated as the ratio between transducer spacing and time of flight, repeating the measurements with the transducers at different distances apart. In this study, the transmitter was kept fixed, and the receiver was placed at a distance of 50, 100, 200, and 300 mm (Fig. 11). Three readings were taken for each position of the transducers, and the velocities of the P- and R-waves were obtained by regression analysis as the slope of the best straight line drawn through

the points (Fig. 12). The correlation coefficients obtained for the linear equations were, in all the samples, higher than 0.98, evidencing a good quality of the registered data.

The relationship between the R-wave and P-wave velocities is based on the fundamental physics of elasticity and elastic wave motion [29]. According to this theory, the relationship between the parameters of elasticity and the velocity of wave propagations can be expressed by Eqs. (1) and (2). The wave velocities obtained for the five tests are reported in

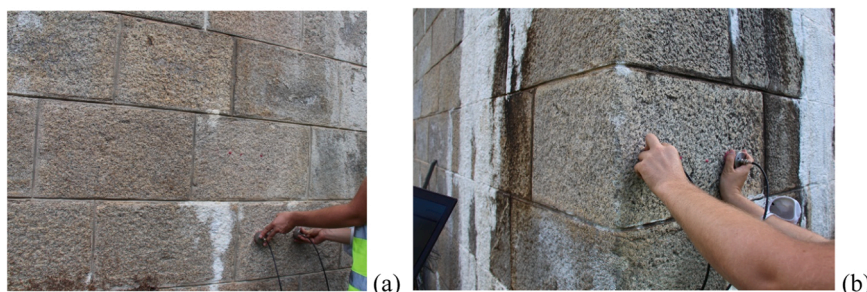


Fig. 11. Ultrasonic tests carried out on the pier's central (a) and corner (b) parts at different positions of the transducers with increasing distance.

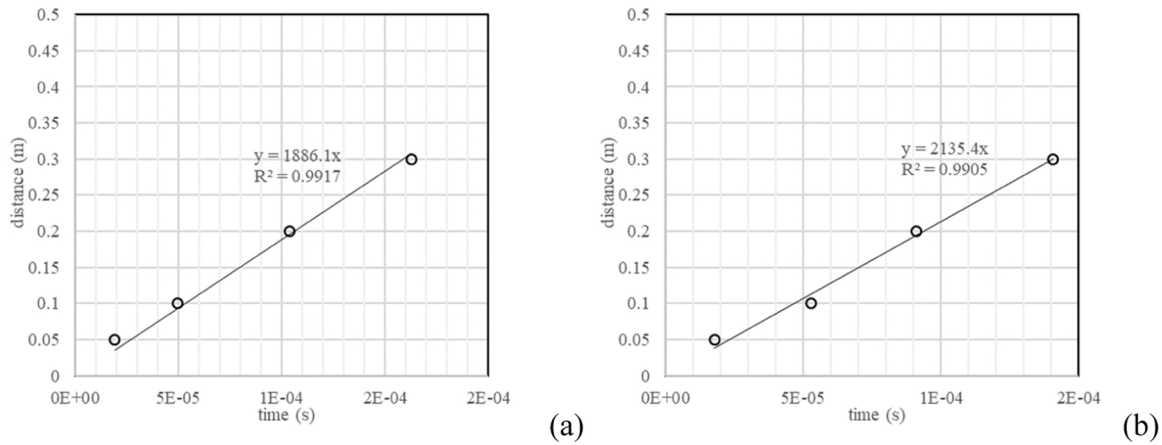


Fig. 12. Correlation between distance and propagation time for evaluating the R-wave velocity of test (a) US-1 and (b) US-2.

the first two columns of Table 3.

$$\frac{v_p}{v_R} = \sqrt{\frac{2(1-\nu)(1+\nu)^2}{(1-2\nu)(0.87+1.12\nu)^2}} \quad (1)$$

$$v_p = \sqrt{\frac{E}{\rho} \frac{(1-\nu)}{(1+\nu)(1-2\nu)}} \quad (2)$$

For all examined blocks, the ratio between the P-wave and R-wave velocities is 1.791, which corresponds to a Poisson's ratio ( $\nu$ ) of 0.2 by Eq. (1). The dynamic modulus of elasticity ( $E$ ) is evaluated using Eq. (2) and assuming a density of  $\rho=2500 \text{ kg/m}^3$ . The results are reported in the third column of Table 3. The obtained values show a reasonable homogeneity (a coefficient of variation, COV, of 14 % based on the five investigated stones). This variability can be justified by some local degradation affecting the external surface of the stone.

The average P-wave velocity is approximately 3300 m/s, which is in the lower range for granite stones [29]. Stone 3 showed particularly low velocities, which may indicate a higher level of deterioration. The average P-wave velocity results in an average dynamic modulus of elasticity of approximately 24 GPa, also in the lower range of values found in the literature for granite stones [30].

### 3.2.2. Impact-echo tests on stone blocks

Impact-echo tests were performed at the exact locations where ultrasonic tests were executed to estimate the thickness of the facing stones. This technique consists of generating an acoustic P-wave using an impact hammer and measuring the accelerations at a point very close to the impact point (Fig. 13). The generated wave propagates into the object undergoing multiple reflections between the tested surface and the opposite surface [31]. This gives rise to a periodical arrival whose frequency ( $f$ ) (i.e. the inverse of the time it takes the wave to go and return to the same point) can be expressed as a function of the thickness of the stone ( $w$ ) by Eq. (3), where  $v_p$  is the P-wave velocity previously estimated by ultrasonic tests and  $\Delta t$  is the travel time. The inverse of Eq. (3) provides an estimation of the thickness  $w$ , given the frequency  $f$  and

the velocity  $v_p$ .

$$f = \frac{1}{\Delta t} = \frac{v_p}{2w} \quad (3)$$

The resulting time domain complex waveform is transformed into a frequency domain to identify the dominant frequency related with the thickness of the stone. Fig. 14 shows two clear frequency spectra obtained for stones 2 and 3. However, internal imperfections or an irregular surface of the back of the stones may result in a complex frequency spectrum. In these cases, there may be multiple dominant frequencies and their interpretation may not be clear.

The tests showed overall consistent results as summarised in Table 4. The thickness of the facing stones ranges between 0.4 and 0.7 m with an average of 0.6 m, which is consistent with on-site measurements. Stone 3 shows the lowest thickness (0.4 m), which is also confirmed by the low velocity estimated by the ultrasonic tests. In summary, the combination of ultrasonic and impact-echo tests revealed that the thickness of the facing stone is about 0.60 m, and the P-wave velocity is around 3200 m/s.

### 3.2.3. Direct sonic tests on external masonry wall of pier

After estimating the wave propagation velocity within the stone blocks and the thickness of the external stone masonry layer, direct sonic tests were performed to investigate the characteristics of the infill material of the piers. Specifically, these tests enable the evaluation of the wave propagation velocity throughout the core of the piers, which provides information on the elastic properties of the pier material. Sonic tests by direct transmission involve placing the hammer and the accelerometer at opposite pier surfaces. The wave propagation velocity can be computed by measuring the pier thickness (distance between the hammer and accelerometer), divided by the time between the emission of the input signal by the hammer and its reception by the accelerometer. There is no standard for sonic testing, but the physical principle is the same as that used in the ultrasonic pulse velocity test. Four locations were chosen for direct sonic tests (Fig. 15).

The pier has a rectangular cross-section of approx.  $5.0 \text{ m} \times 7.2 \text{ m}$  at the base, slightly decreasing with the height. Two tests were carried out along the long side (7.2 m): (A) direct sonic test at 0.2 m from the pier edge; and (B) direct sonic test at 1.5 m from the edge. Other two tests were carried out along the short side of the pier (5.0 m) at about the centre of the pier (C1 and C2), as shown in Fig. 15.

Ten hits were performed at each location. The results are summarised in Table 5, where the coefficient of variation (CoV) calculated for each location is also reported. The low coefficients of variation confirmed the good quality of the signal obtained at the receiver accelerometer. All positions show significantly high velocity (average velocity over 4000 m/s). Note that this velocity is higher than the

Table 3  
Velocities and dynamic modulus of elasticity on the masonry pier stones obtained by ultrasonic tests using the indirect transmission method.

Test	$v_R$ (m/s)	$v_p$ (m/s)	$E$ (GPa)
US-1	1886	3378	25.68
US-2	2135	3825	32.92
US-3	1478	2647	15.76
US-4	1998	3579	28.82
US-5	1687	3022	20.55
Average (COV)	1837 (14 %)	3290 (14 %)	24.75 (27 %)



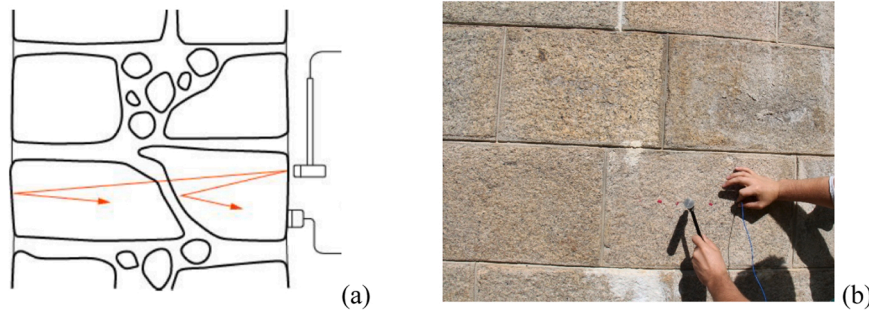


Fig. 13. (a) Schematic drawing of the impact-echo test principles (reflections will occur at the different boundaries of the analysed object); (b) impact-echo tests carried out on-site.

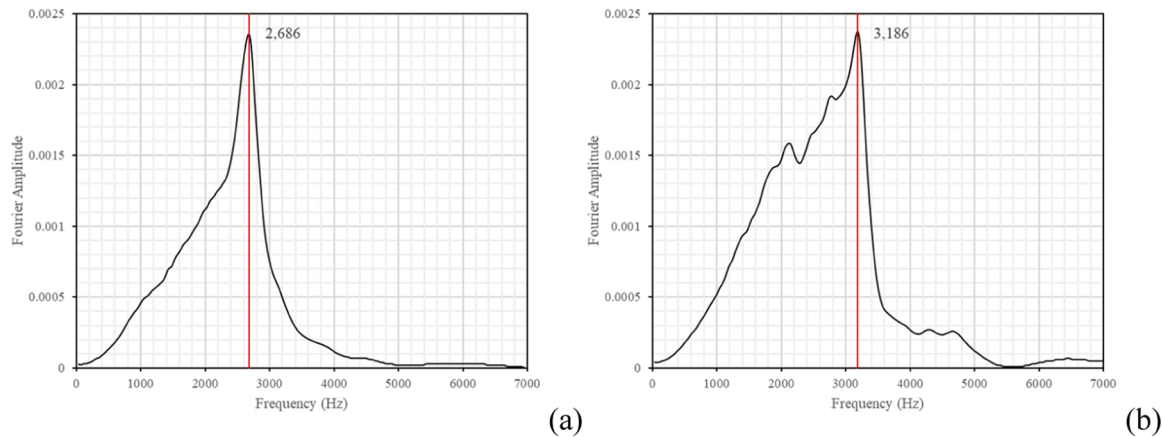


Fig. 14. Examples of frequency spectra obtained from (a) Stone 2; and (b) Stone 3.

**Table 4**  
Velocities obtained in the Impact-echo tests carried out at the masonry pier with the indirect transmission method.

	$v_p$ (m/s)	$f$ (Hz)	$w$ (m)
IE-1	3378	2520	0.67
IE-2	3825	2680	0.71
IE-3	2647	3205	0.41
IE-4	3579	3215	0.56
IE-5	3022	2285	0.66
Average (COV)	3290 (14 %)	2781 (15 %)	0.60 (20 %)

velocity estimated for the stone (average velocity of 3290 m/s). It indicates that the core is composed of a good-quality homogeneous material with no voids.

The velocity at location A is slightly lower than at other positions, which should be due to the specific test location close to the pier edge. In this case, the wave could have partially gone through the external stone masonry layer. Thus, the lower velocity at location A confirms that the wave velocity through the inner core is greater than that of the wave going through the facing stones. Note that the masonry joints tend to lower the velocity of the wave. Given the velocity of the P-waves through the stones ( $v_{p,block}$ ) and the block thickness ( $w$ ), the average velocity of the P-waves through the infill material ( $v_{p,infill}$ ) can be evaluated using Eq. (4), where  $v_p$  is the velocity of the P-waves measured in the test and  $L$  represents the distance between the hammer and the accelerometer. The results are reported in Table 6.

$$v_{p,infill} = \frac{v_p L - 2v_{p,block} w}{(L - 2w)} \quad (4)$$

In summary, the results of the direct sonic tests on the masonry pier seem to indicate that the inner core is composed of a solid homogeneous

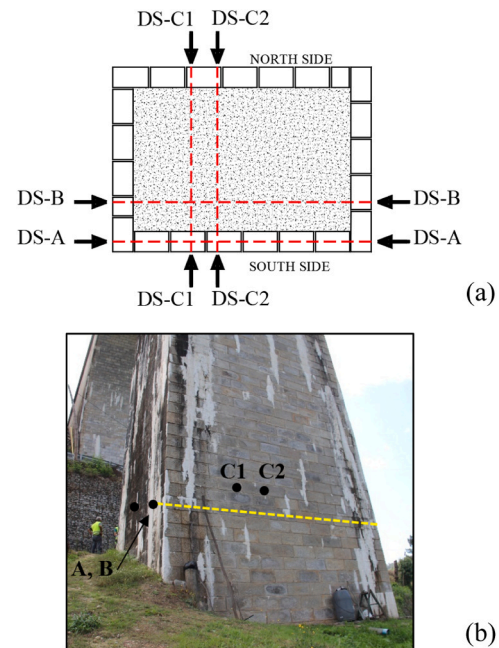


Fig. 15. (a) Pier cross section and (b) external view to the pier with direct sonic test locations.

material with no significant voids. Velocities close to 4400 m/s are typical of sound concrete (3000–4500 m/s [32]).

The combined use of impact-echo and ultrasonic and sonic testing indicates that the pier is composed of approximately a facing stone

**Table 5**  
Velocities obtained in the direct sonic tests carried out at the masonry pier.

	A (CoV)	B (CoV)	C1 (CoV)	C2 (CoV)
$v_p$ (m/s)	3760 (1.4 %)	4080 (3.2 %)	4460 (1.1 %)	4215 (0.6 %)

**Table 6**  
Estimation of the velocity of the P-waves through the pier infill material.

Direction	$v_p$ (m/s)	$L$ (m)	$v_{p,block}$ (m/s)	$w$ (m)	$v_{p,infill}$ (m/s)
Longitudinal (test B)	4080	5.0	3290	0.6	4329
Transversal (Tests C1, C2)	4338	7.2	3290	0.6	4548
Average					4438

masonry layer (0.6 m thick) and an inner core of a homogenous concrete material with no significant voids. Using Eq. (1), assuming a Poisson's ratio equal to 0.2 and a density of  $2400 \text{ kg/m}^3$ , the dynamic modulus of the infill material is estimated equal to 42 GPa. Note that the static modulus is typically smaller than the dynamic modulus. Experimental studies from the literature estimate that the ratio between the two moduli is around 1.2 [33,34], which results in an estimated static modulus of elasticity of about 35 GPa. This value reveals a good quality concrete in the inner core of the piers.

**3.2.4. Indirect sonic tests on external wall of pier**

Indirect sonic tests were carried out to estimate the elastic properties of the stone masonry external layer of the pier. The procedure for implementing the tests starts with the definition of a suitable grid of points on the investigated wall and the subsequent positioning of the hammer and accelerometer on the same surface (indirect transmission). The wave propagation velocity is computed by measuring the time between the emission of the input signal by the hammer and its reception by the accelerometer, and the distance between them. As previously mentioned, indirect sonic tests provide both primary waves (P waves) velocity ( $v_p$ ) and surface or Rayleigh waves (R waves) velocity ( $v_R$ ), which have different travel times (Fig. 10). As previously discussed for the ultrasonic testing, knowing the density of the material ( $\rho$ ), the relationship among the velocities of both waves can be correlated with the dynamic modulus ( $E$ ) and the Poisson's ratio ( $\nu$ ) by using Eq. (1) and (2). However, it should be noted that these expressions were originally developed for homogeneous isotropic elastic materials, which is not the case of stone masonry. Moreover, the dynamic modulus of elasticity is usually higher than Young's static modulus recommended in the codes and typically used in structural analysis. Thus, the expressions must be used carefully, acknowledging that the results are an approximate estimation of the mechanical properties.

The facing stone masonry wall under evaluation is a regular ashlar granite masonry wall in an overall good state of conservation, despite the visible accumulation of salt crusts on the exterior surfaces. Fig. 16 shows the 3x3 grid layout adopted for the tests with a separation of 0.7 m between points. At each position, the hammer and the accelerometer were aligned vertically and horizontally to capture a possible anisotropic behaviour of the masonry, with 0.7 m (e.g. 1-4/1-2) and 1.4 m (e.g. 1-3/1.7) distance, resulting in a total of 20 tests. The results are summarized in Table 7. It is noted that the identification of the arrival of the P-wave was clear for these tests and, therefore, only these results are reported. The results show a significant homogeneity with an overall low variability. Lower velocities are consistently observed when the test points are closer (0.7 m distance). This may be because the wave does not travel in a straight vertical or horizontal path, but instead follows the fastest route, which could involve passing partially through the infill (where higher velocities are observed) and avoiding crossing multiple mortar joints.

The average P-wave velocity ( $v_p$ ) is 2300 m/s for the vertical

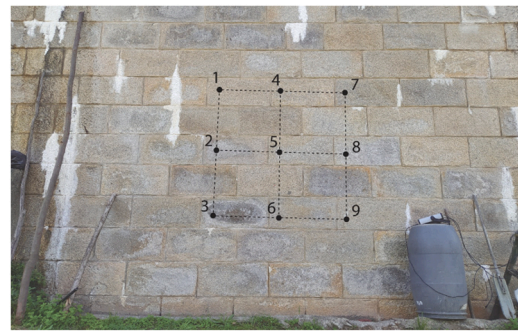


**Fig. 16.** Grid applied for the indirect sonic tests performed on the northern wall of the pier.

**Table 7**  
Velocities obtained direct sonic tests carried out at the external layer of the masonry pier.

Grid	Path	Direction	$v_p$ (m/s)	
A	1-2	Vertical	1690	
	1-3		2125	
	4-5		2350	
	4-6		2445	
	7-8		2085	
	7-9		2390	
	Average (COV)	2180 (13 %)		
	B	2-5	Horizontal	2130
		2-8		2285
		3-6		1700
3-9		2520		
Average (COV)		2160 (16 %)		
1-2		Vertical		2460
1-3			2255	
4-5			2280	
4-6			2770	
7-8			2190	
7-9	2580			
Average (COV)	2420 (9 %)			
Total	Average (COV)	Horizontal	2390	
	Average (COV)	Vertical	2300 (12 %)	
	Average (COV)	Horizontal	2190 (12 %)	

direction and 2190 m/s for the horizontal direction, denoting a good quality of masonry, which was expected from the well-preserved regular granite masonry wall observed on-site.

Moreover, the velocity in the horizontal direction is very similar to that obtained in the vertical direction, indicating a low level of masonry anisotropy. Furthermore, the low variability of the results (CoV lower than 20 %) highlights that the masonry is significantly homogeneous.

Assuming a Poisson's ratio of 0.25 and a  $2300 \text{ kg/m}^3$  density, the masonry dynamic modulus of elasticity is estimated using Eq. (1) and (2). In the literature, values between 1.2 and 1.3 are generally accepted for the ratio between static and dynamic modulus of elasticity of masonry [35,36]. However, recent studies performed on masonry panels evidenced lower values [17]; therefore, in this study, a value of 1.1 is adopted.

The results for the modulus of elasticity are expressed in probability terms using a lognormal distribution based on the average value and standard deviation (STD), which will facilitate future probabilistic assessments of the bridge structural safety. Fig. 17 shows the lognormal distribution of the estimated static modulus of elasticity for the vertical (Fig. 17a) and horizontal directions (Fig. 17b).

The mean values of the static masonry moduli of elasticity resulted in 9.4 GPa (STD 2.04 GPa) and 8.5 GPa (STD 1.86 GPa) in the vertical and

horizontal directions, respectively, which are within the expected range of values for ashlar granite masonry [30].

### 3.3. Ground-penetrating radar

Ground-penetrating radar (GPR) [26] is a powerful tool for characterizing the internal morphology of construction elements and providing information on homogeneity, structural configuration, voids, and irregularities [37]. The method is based on the emission of high-frequency electromagnetic waves (radar waves) into a structural element using a dipole antenna. The wave propagates through the material, and part of it is reflected in correspondence of discontinuities in the dielectric properties of the medium, revealing defects, cracks, or interfaces between different materials, namely the backside of a wall or a stone. The time between the emission and reception of the reflected waves can be measured and it allows the determination of the location and depth of the observed anomaly given the propagation velocity of the radar waves within the media. According to the literature, the average radar-wave velocity in masonry is 12–14 cm/ns [30]. In this study, GPR tests were performed to estimate the thickness of the piers and spandrel walls using the RAMAC/GPR system from MALA (Guideline Geo) and a 1600 MHz antenna. A series of GPR profiles were carried out at the first pier from the southern side of the bridge and the walls of the bridge abutments (Fig. 18).

Fig. 19a shows a radargram in the horizontal direction at the wall of the southern bridge abutment. There are clear reflections at a depth of 0.4–0.6 m, which seems to imply the opposite surface of the facing stones. The antenna was moved over three different stones and show a slightly varying thickness within this 0.4–0.6 m range. There are no reflections after the facing stone layer, indicating that either the signal is significantly attenuated after the stone or the presence of a homogeneous material. Fig. 19b shows the vertical scan of the bridge abutment and very similar conclusions can be extracted. Again, there are clear reflections at a depth of 0.35–0.55 m, indicating the opposite surface of the facing stones. The antenna was moved over five different stones that also show a slightly varying thickness. There are also no reflections after the facing stone layer.

Fig. 20a shows a radargram in the vertical direction at the masonry pier of the bridge. It is similar to the ones obtained from the bridge abutment. There are clear reflections at a depth of 0.45–0.55 m, which seems to indicate the opposite surface of the facing stone layer. The antenna was moved over six different stones, which show a varying thickness, but the variations are lesser than the ones observed at the abutment. It is noted that the depth of the stones measured with the impact-echo tests was 0.6 m (average) and varied between 0.4 and 0.7 m. The range obtained by the two techniques independently is thus similar. There are again no reflections after the facing stone layer, which could indicate the presence of a homogeneous material or that the signal is significantly attenuated after the stone. Finally, Fig. 20b shows a radargram carried out in the vertical direction at the edge of the

masonry pier. In this case, the depth of the stones is known because the antenna passes over the external facing stone masonry wall instead of the inner core.

The radargram in Fig. 20b is significantly different from that in Fig. 20a, and it is consistent with the block-masonry arrangement observed on site. This confirms that (i) the inner core is not made of regular stone masonry; (ii) the external layer is composed of a single-facing stone layer. The presence of a homogeneous material after a facing stone layer also matches the results of sonic and ultrasonic investigations.

## 4. Numerical model

A 3D numerical model for the entire bridge (Fig. 21), including external masonry parts and infill material layers has been developed using the finite element (FE) code ADAPTIC [38]. The numerical model was generated by a recently developed parametric modelling tool for masonry arch bridges [39], which corresponds to an add-on component to the commercial 3D computer graphics and computer-aided design application software Rhino and its parametric environment Grasshopper [40]. The tool defines independent parametrically defined components (arch barrel, multi-layered backing/backfill domain, spandrel walls, and composite piers) that are further connected to form a bridge model. This approach allows for a flexible definition of model fidelity, where each component can be modelled at either meso- or macroscale. These capabilities are further enhanced by the possibility of incorporating nonlinear interfaces acting between each of the bridge masonry parts (i. e., vaults to spandrel walls) or between masonry and backfill, also allowing for non-conforming mesh generation [41]. The tool automatically introduces efficient model partitioning enabling parallel computation [42] which is essential to improve computational efficiency when analysing large structures. Finally, fully fixed boundary conditions are considered at the base of the piers and at the two vertical ends of the viaduct.

According to the results from the in-situ tests, the piers are modelled considering perimeter masonry walls and inner concrete filling. The barrel vaults are modelled with variable thickness to reproduce the effective internal structure of the bridge. This geometry is extended to the entire transversal dimension of the bridge, approximating the actual geometry of the external walls characterised by constant arch thickness. Fig. 4. Quadratic 20-noded continuum solid elements are employed in the model. Fig. 21a shows the mesh discretisation used for the bridge external masonry walls (piers, vaults, and spandrel walls); while the inner core, backfill, and backing layers are shown in Fig. 21b.

Linear-elastic 16-noded interface elements [43] are employed to describe the contact regions, as shown in Fig. 21c. This hybrid continuum-discrete approach allows for the description of the elastic deformability of the contact regions.

A recently developed anisotropic macroscale continuum model, implemented in the software ADAPTIC [38], is used to represent the

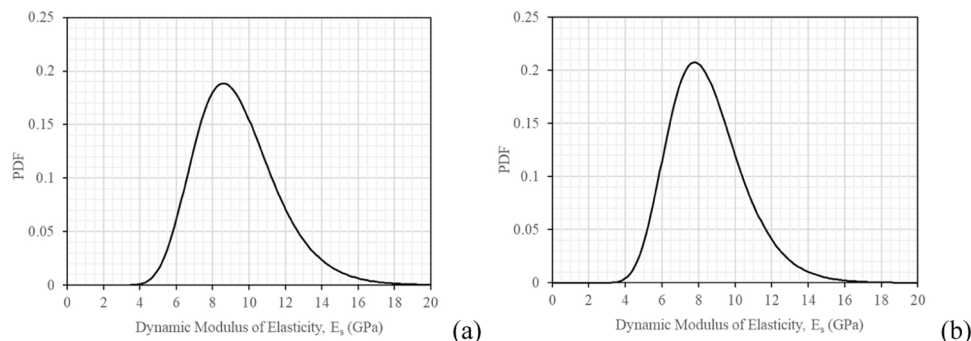


Fig. 17. Lognormal distribution of the static modulus of elasticity for the: (a) vertical and (b) horizontal directions.





Fig. 18. GPR tests at two different locations of the bridge.

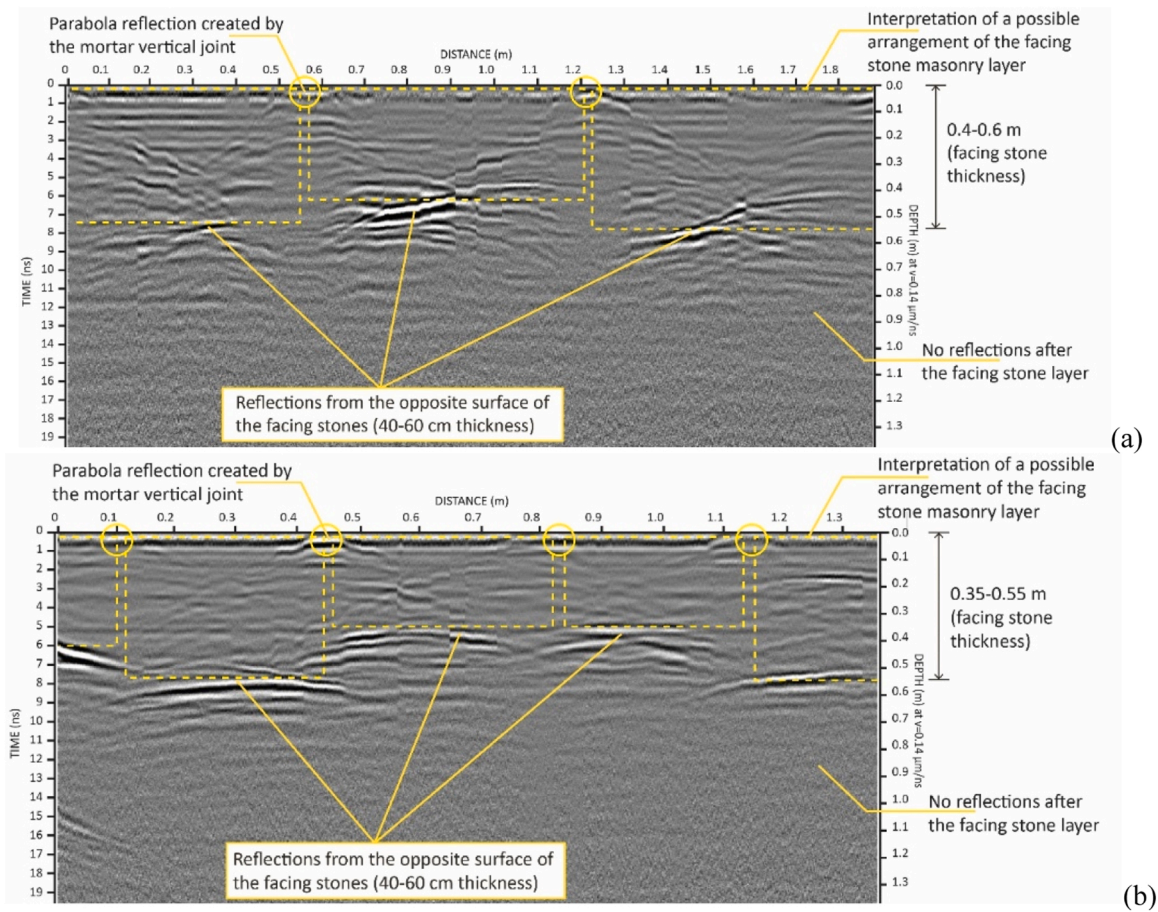


Fig. 19. GPR (a) horizontal and (b) vertical scan at the wall of the bridge abutment.

masonry components of the bridge structure: arches, lateral walls and the external walls of the piers. The masonry material model is based upon a two-scale description, where a mesh of solid finite elements is used at the macro-level (Fig. 22a). Each solid element is coupled at the level of integration Gauss points with an orthotropic micro-level discontinuous representation with distributed *internal layers* (ILs), allowing for both the elastic and nonlinear behaviour of masonry (Fig. 22b) [44]. Three local material directions ( $x, y, z$ ) characterise the model, where  $x$  and  $y$  identify the two in-plane directions orthogonal and parallel to the mortar bed joints, while  $z$  identifies the out-of-plane direction when modelling a masonry wall component or the radial direction in the case of curved elements. Simple rules are used to evaluate the deformations of the internal layers from the macroscopic deformations by following the procedure described in [44]. The generic

$i$ -th ( $i=x, y, z$ ) internal layer is characterised by three deformation parameters,  $(\epsilon_i, \gamma_{i,k}, \gamma_{i,l})$ , where  $\epsilon_i$  is the normal deformation, and  $\gamma_{i,k}, \gamma_{i,l}$  (with  $k, l=x, y, z$  and  $k, l \neq i$ ) the shear deformations in the two local directions parallel to the internal plane, parallel and orthogonal to the masonry plane (or the local tangent panel in the case of curved elements) [11]. Three internal stresses  $(\sigma_i, \tau_{i,k}, \tau_{i,l})$ , dual to the internal deformations, are independently evaluated by integrating the constitutive laws of each internal layer. In this study, the elastic constitutive behaviour of the layer is governed by a diagonal stiffness matrix  $\mathbf{k}_i = \text{diag}\{E_{ni}, E_{ik}, E_{il}\}$ . Therefore, in the elastic field, the model is characterised by three normal moduli ( $E_{ni}$ ), two in-plane shear moduli ( $E_{xz}, E_{zx}$ ), and four out-of-plane shear moduli ( $E_{zy}, E_{yz}, E_{xy}, E_{yx}$ ). The local stiffness matrix, evaluated at each Gauss point, is obtained by imposing internal Cauchy conditions, as described in [44]. Finally, linear elastic

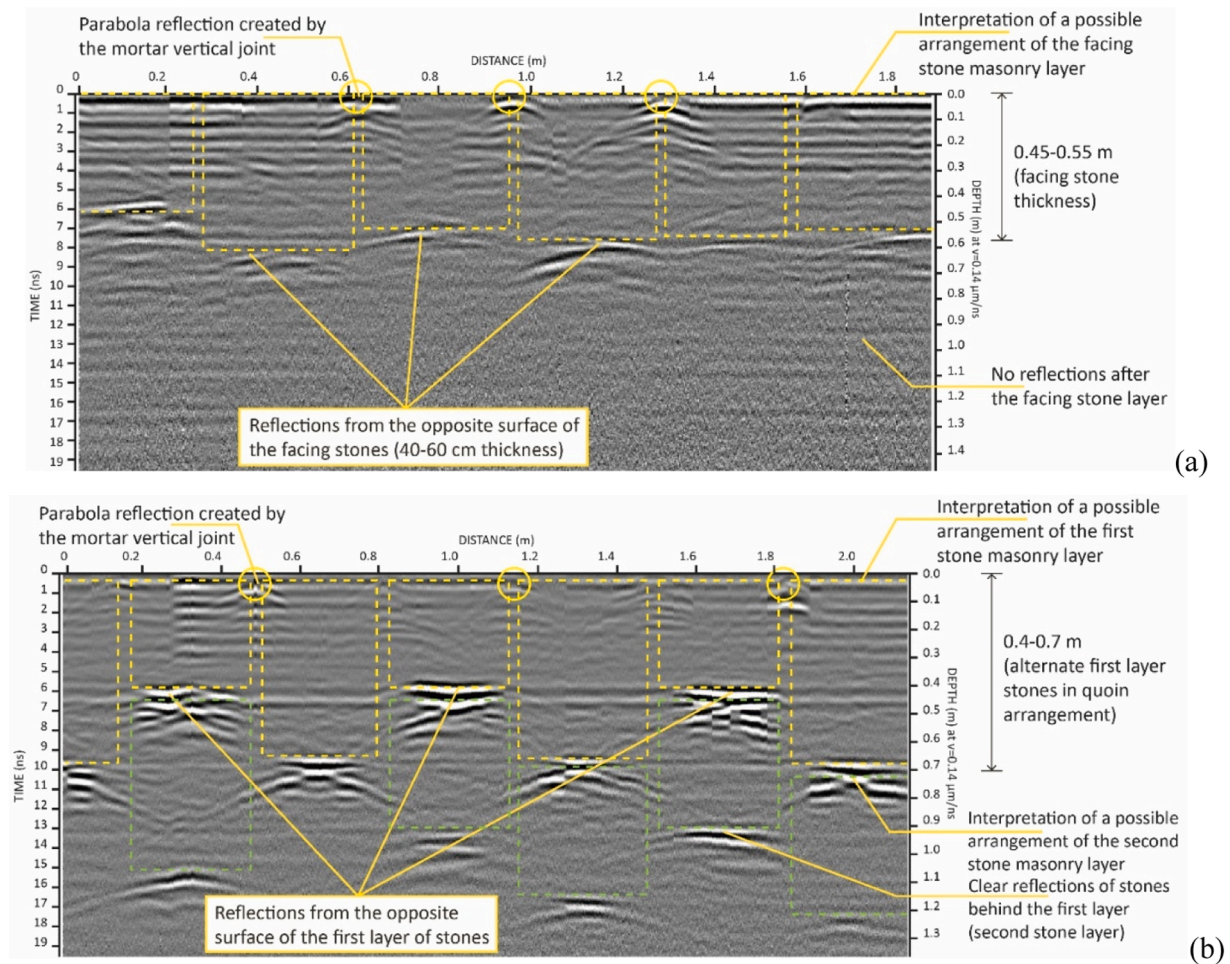


Fig. 20. GPR vertical scan at the (a) edge and (b) corner of the bridge masonry pier.

Cauchy models are adopted for the backing and backfill layers and the inner parts of the piers.

The adopted model has a significant advantage in accounting for the masonry bond with much lower computational effort compared to standard two-scale strategies. In the proposed model, the periodic cell is used to calibrate the properties of the internal layers, eliminating the need to explicitly solve representative periodic cells at each integration point [44]. The computational performance of the proposed modeling strategy has been evaluated in [11] and [44] in terms of computing time, which resulted in approximately 10 % of that required by more refined mesoscale models.

## 5. Experiment-based model calibration

A preliminary calibration of the model elastic material parameters is based on the results from the material (local) NDTs. The accuracy of the calibrated model in the elastic range is checked by comparing the predicted main modes of vibration of the viaduct against the results from the experimental dynamic identification in terms of frequency errors (%) and MAC indexes. Subsequently, parametric analyses are performed to evaluate the influence of the main material properties on the bridge dynamic characteristics. The results presented in this section represent the starting point for a more advanced calibration in Section 6, where optimisation algorithms and statistic inference methods are employed to evaluate the optimal set of model parameters.

### 5.1. Evaluation of the material parameters

The elastic material parameters for masonry, pier-fill, backfill and backing layers are determined according to the results from the in-situ NDTs, data from the literature, historical documentation and straight-forward homogenisation [11,44]. The results are summarised in Table 8. More specifically, the NDTs allowed the evaluation of the Young's modulus for the inner material of the piers ( $E_{pr}=35$  GPa). The properties for the backing and backfill were assumed based on the historical documentation available for the investigated bridge and for similar bridges built in the same period [21]. More specifically, the backing is assumed to be made of poor concrete with Young's modulus of 25 GPa, while the backfill is supposed to be made of an inconsistent material (soil or irregular masonry) with Young's modulus of 1.5 GPa.

The Young's modulus of masonry in the direction parallel to the bed joints ( $E_{mp}$ ) is assumed equal to the average value obtained from the indirect sonic tests on the piers along the horizontal direction ( $E_{test,h} = 8.5$  GPa). On the contrary, the modulus obtained by the same tests conducted in the vertical direction ( $E_{test,v} = 9.4$  GPa) is not directly used to characterise the masonry in the direction orthogonal to the joints ( $E_{mo}$ ), since the experimental value does not account for Poisson effects. Instead,  $E_{test,v}$  is used to estimate the Young's modulus of the mortar ( $E_m$ ) by considering an homogeneous medium with stiffness equivalent to the stiffness of the stone blocks and the masonry joints arranged in series, using Eq. (5), where  $h_b = 300$  mm is the average height of the blocks,  $h_m = 10$  mm is the thickness of the mortar joints and  $E_b = 24$  GPa is the Young's modulus of the stone blocks. It results in  $E_m = 480$  MPa.



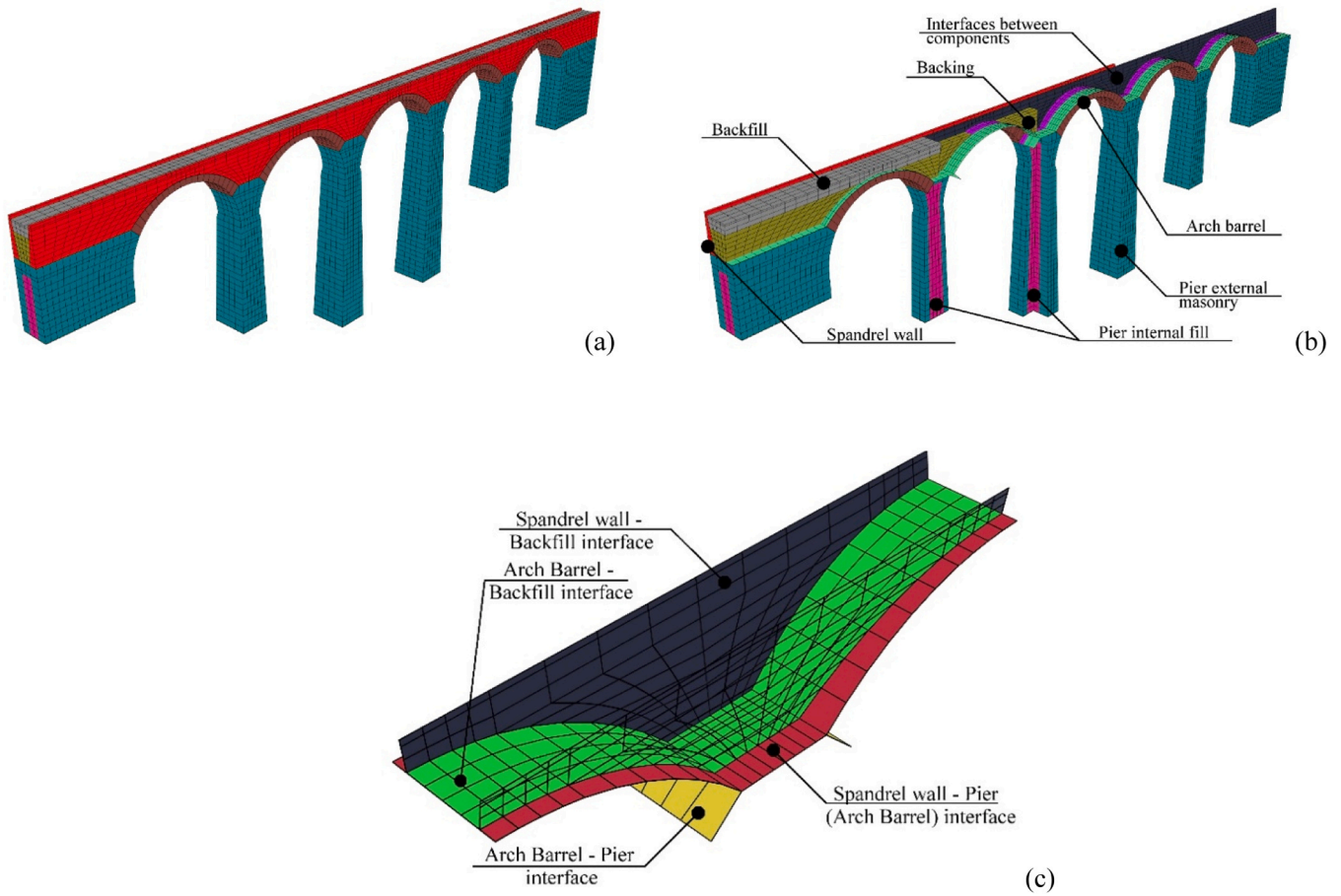


Fig. 21. 3D FE viaduct model: (a) external and (b) internal structure; (c) interface elements.

$$\frac{1}{E_{test,v}} = \frac{h_b}{E_b(h_m + h_b)} + \frac{h_m}{E_m(h_m + h_b)} \quad (5)$$

Then, according to the procedure described in [11], the macroscopic Young's modulus of masonry in the direction orthogonal to the joints ( $E_{mo}$ ) is evaluated by Eq. (6), where  $\nu_b = \nu_m = 0.2$  are the Poisson's coefficients of the blocks and mortar. It leads to  $E_{mo} = 10$  GPa. Finally, the shear modulus of masonry is evaluated using Eq. (7) [11].

$$E_{mo} = \left[ \frac{h_b}{E_b(h_m + h_b)} + \frac{h_m}{E_m(h_m + h_b)} - \frac{h_b h_m}{E_{mb}(h_m + h_b)^2} \left( \frac{\nu_b}{E_b} - \frac{\nu_m}{E_m} \right)^2 \right]^{-1} \quad (6)$$

$$G_m = \left[ \frac{2(1 + \nu_b)h_b}{E_b(h_m + h_b)} + \frac{2(1 + \nu_m)h_m}{E_m(h_m + h_b)} \right]^{-1} \quad (7)$$

### 5.2. Calibration of the masonry model

The macroscopic masonry parameters determined in the previous section have been used to calibrate the macroscale masonry model described in Section 4, and more specifically, the elastic parameters of the Internal Layers (ILs) oriented along the three main material directions ( $x, y, z$ ), where  $x, z$  are the in-plane directions orthogonal and parallel to the bed joints, and  $y$  is the out-of-plane direction (Fig. 22b).

Following the practical calibration procedure described in [11], the Young's moduli of the ILs in the local  $x$  and  $y$  directions are assumed equal to the Young's moduli in these directions: ( $E_{nz} = E_{mo}$ ;  $E_{nx} = E_{mp}$ ); the two in-plane shear modulus of the ILs in the  $x$  and  $z$  directions are assumed  $E_{xz} = E_{zx} = 2G_m$ ; the two out-of-plane shear moduli of ILs in the  $x$  and  $y$  local directions ( $E_{xy} = E_{yx}$ ) and the  $z$  and  $y$  local directions ( $E_{zy} = E_{yz}$ ) are evaluated by combining in series the shear deformability of the

blocks and the mortar joints using Eq. (8), where  $b_b$  and  $h_b$  are the width and height of the bricks. Finally, the normal modulus of IL in the local direction  $z$  ( $E_{nz}$ ) is assumed to be coincident with the Young's modulus of the stone blocks. The complete set of the mechanical parameters for the macromodel are reported in Table 9. Finally, the masonry-backfill interface stiffnesses  $k_n = 60$  kN/mm and  $k_t = 30$  kN/mm are assumed according to [4]. Previous studies [4,11] and preliminary analyses conducted in this study, which are not reported here for the sake of brevity, have confirmed that variations in the stiffness values from those adopted in the literature do not significantly affect the dynamic characteristics of the bridge. Therefore, these parameters are being kept fixed and are not included in the optimization algorithms in order to limit the number of parameters to be optimized.

$$E_{xy} = E_{yx} = 2[G_m G_b (b_b + h_m) / (G_b h_m + G_m b_b)] \quad (8a)$$

$$E_{zy} = E_{yz} = 2[G_m G_b (h_b + h_m) / (G_b h_m + G_m h_b)] \quad (8b)$$

### 5.3. Numerical validation

Numerical simulations with the calibrated viaduct model were conducted to predict the first three natural frequencies, which were compared against the experimental values. It has been decided to exclude the fourth experimental mode from the comparisons because it has been obtained processing the data from a single accelerometer, and therefore it is unsuitable to evaluate the modal shape.

The percentage errors are reported in Table 10, while the predicted mode shapes and the MAC indexes measuring the consistency between the numerical and experimental vibration modes are indicated in Fig. 23. The fourth experimental vibration mode, which is characterised



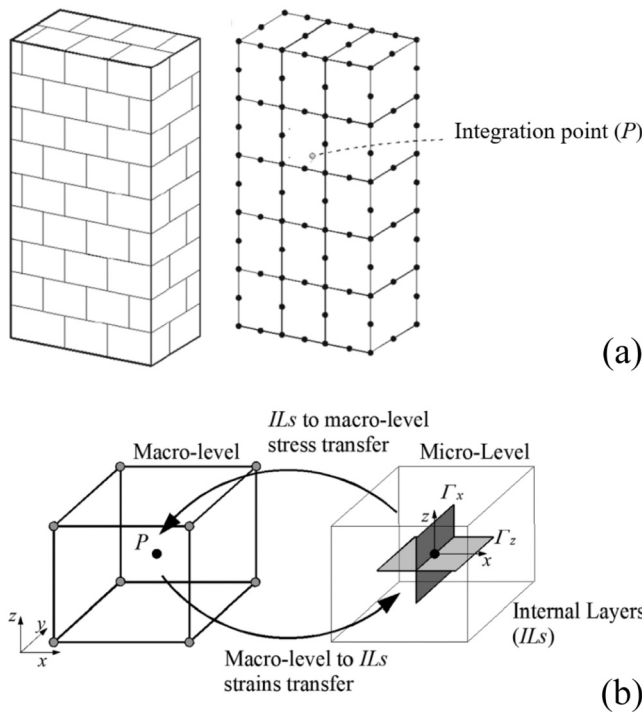


Fig. 22. Schematic representation of the two-scale description of the masonry macroscale model [44]: (a) continuum FEM description at the macro-scale level; (b) transfer of information from the macroscale level to the internal layers.

by a significant component of vertical acceleration, is not considered here since it has been identified using a single accelerometer. Table 10 confirms that the first numerical frequency fits well with the experimental results, with errors ranging between 3 % and 8 %. On the contrary, the second and the third frequencies show higher errors between 13 % and 15 %. The initial material properties directly obtained from the sonic inspections seem slightly underestimated, as the experimental frequencies are higher than the numerical ones. This may be due to the fact that the values of Poisson’s ratio and density used to obtain Young’s modulus were assumed and not measured. Moreover, the chosen ratio between the static and dynamic moduli is also based on empirical data and could be lower than the actual value. Finally, good consistency is observed in terms of mode shapes for all three fundamental modes with MAC values close to or greater than 0.9, evidencing a good agreement between the numerical and experimental results.

5.4. Parametric analyses

The results reported evidence a good agreement between numerical and experimental data, even when using a straightforward model calibration procedure. Indeed, the reached level of approximation is judged suitable for engineering applications, considering all uncertainties involved in modelling historical bridges. However, in addition to accuracy, assessing the model sensitivity to the main material parameters is fundamental to evaluating its robustness against the variation of material parameters. With this aim, a sensitivity analysis has been conducted by varying the eight parameters that affect the bridge response most

Table 8 Material mechanical parameters based on the in-situ tests.

Masonry				Pier infill (Strong Concrete)			Backing (Poor Concrete)			Backfill (Incoherent material)		
$E_{mo}$ (GPa)	$E_{mp}$ (GPa)	$G_m$ (GPa)	$\rho_m$ (kN/m <sup>3</sup> )	$E_{pr}$ (GPa)	$\nu_{pr}$ (-)	$\rho_{pr}$ (kN/m <sup>3</sup> )	$E_{bk}$ (GPa)	$\nu_{bk}$ (-)	$\rho_{bk}$ (kN/m <sup>3</sup> )	$E_{bf}$ (GPa)	$\nu_{bf}$ (-)	$\rho_{bf}$ (kN/m <sup>3</sup> )
10	8.5	3.9	23	35	0.20	24	25	0.20	23	1.5	0.2	22

significantly. More in detail, the investigated parameters include:

- Three masonry properties, namely the Young’s modulus orthogonal to the bed joints ( $E_{nz}$ ), the anisotropy ratio ( $E_{nx}/E_{nz}$ ) by varying the Young’s modulus parallel to the joints and the in-plane shear deformability ratio ( $E_{xz}/E_{nz}$ ) by varying the moduli  $E_{xz}=E_{zx}$ .
- Two parameters that characterise the inner fill material of piers, namely the Young’s modulus ( $E_{pr}$ ) and the Poisson ratio ( $\nu_{pr}$ ).
- Three backfill/backing parameters, namely the Young’s moduli of backfill ( $E_{bf}$ ) and backing ( $E_{bk}$ ), and the Poisson’s ratios ( $\nu_{bf} = \nu_{bk}$ ).

Each parameter is changed one at the time within the upper and lower bounds reported in Table 11, while keeping all the other parameters constant and equal to the reference value in Table 8. The ranges of material parameters considered in the analyses are chosen according to specific literature [45] to cover a wide range of material scenarios and possible factors and defects potentially affecting the material properties, including pre-existing damage. For this reason, they are not centered on the values resulting from the in-situ tests, which are within the considered range in all cases. More specifically, the Young’s modulus of masonry is varied from 2 GPa to 20 GPa according to [30]. The concrete fill material in the piers, as indicated by the sonic tests, is varied from 10 GPa to 40 GPa. The Young’s moduli of backing and backfill materials are varied in the ranges 10–35 GPa and 0.5–1.5 GPa assuming a lower bound of poor concrete and an incoherent material, respectively.

The results of the parametric analyses are shown in Fig. 24 for the masonry parameters, in Fig. 25 for the fill parameters of the piers, and in Fig. 26 for the backfill and backing parameters. These figures show the frequency percentage error as the envelopes for the different methods used for the modal identification, and the MAC indexes for the three fundamental modes of the bridge. Generally, the frequency error showed much higher variability than the MAC, which is about 0.9 for most of the parameter ranges. However, it can be observed that, in some cases, a reduction of the frequency errors corresponds to a decrease in the MAC index, confirming the potential benefit of using multi-objective optimisation with frequency errors and MAC values as target functions

Table 9 Elastic masonry parameters employed to calibrate the equivalent continuum macro-model (GPa).

In-plane interfaces			Out-of-plane interfaces		
$E_{nx}$	$E_{nz}$	$E_{xz}=E_{zx}$	$E_{nz}$	$E_{xy} = E_{yx}$	$E_{zy} = E_{yz}$
10	8.5	7.8	24	11	7.8

Table 10 Numerical frequencies.

	Frequency (Hz)		Error (%)		
	Experimental		Numerical		
	Lower bound	Upper bound	Lower bound	Upper bound	
First mode	1.62	1.70	1.56	3.7	8.1
Second mode	2.69	2.72	2.34	13.2	13.9
Third mode	3.95	4.00	3.40	13.9	14.9

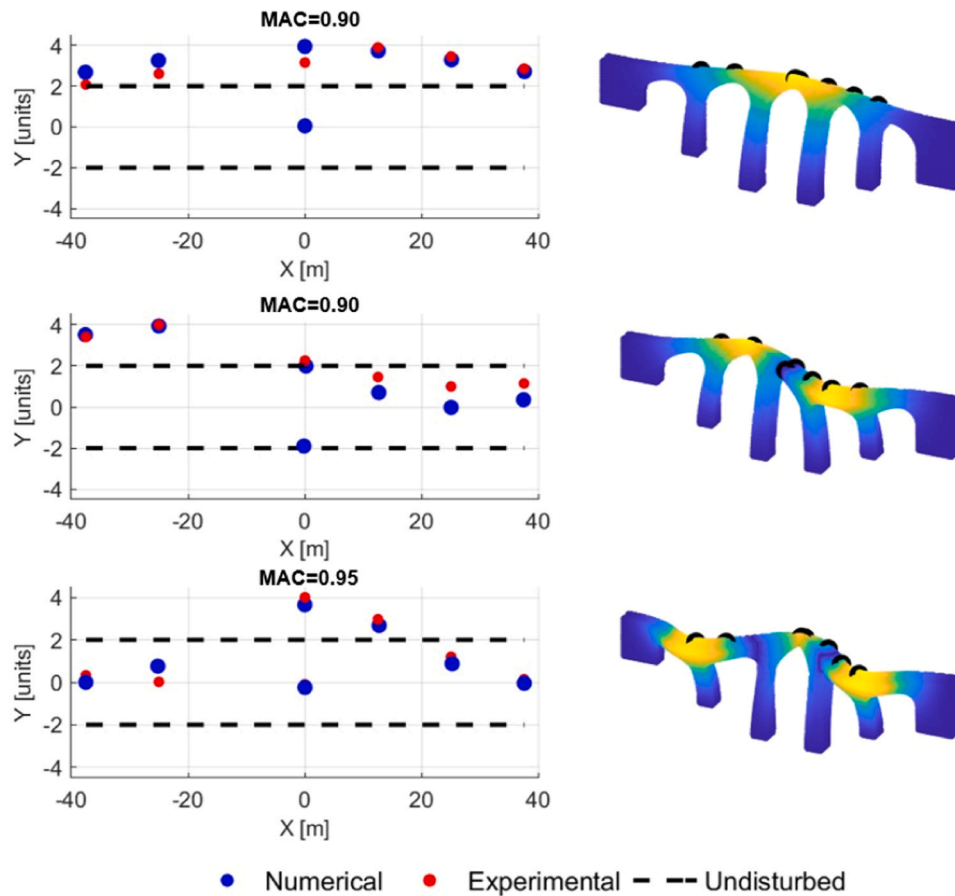


Fig. 23. Predicted numerical and experimental mode shape.

**Table 11**  
Ranges of material parameters considered in the parametric analyses.

	Masonry			Pier Infill		Backfill/Backing		
	$E_{ny}$ (GPa)	$E_{nx}/E_{ny}$ (-)	$E_{xy}/E_{ny}$ (-)	$E_{pr}$ (GPa)	$\nu_{pr}$ (-)	$E_{bk}$ (GPa)	$E_{bf}$ (GPa)	$\nu_{bf} = \nu_{bk}$ (-)
Upper bound	20	1.5	1.5	40	0.35	35	5.0	0.35
Lower bound	1.5	0.5	0.5	10	0.15	10	0.5	0.15

for an improved model calibration.

Fig. 24 shows that all the considered masonry parameters significantly affect the bridge dynamic properties. It can be observed that varying the Young’s modulus  $E_{nz}$  from 5 to 20 GPa leads to an error on the first frequency ranging from approximately 25–0 % while the error for second and third frequencies varies from 35 % to 0 %. Also, the masonry anisotropy ( $E_{nx}/E_{nz}$ ) has a significant effect on the modes, evidencing that the use of isotropic models, often employed in research and engineering applications, may lead to inaccurate prediction of the dynamic response.

It is also worth highlighting the influence of the masonry in-plane shear deformability ( $E_{xz}/E_{nz}$ ). This result can be explained due to the shear deformations of the barrel vaults involved in the transversal deformation of the bridge, characterising all three fundamental modes of the structure.

The sensitivity analysis confirms that the Young’s modulus of the pier fill material has a major effect on the frequencies reducing prediction error for the first frequency by up to 25 % and second and third by up to 13 % (Fig. 25).

On the contrary, a lower influence of the backfill and backing material is observed. The variation of the Young’s moduli of backing (10 – 35 GPa) and backfill (0.5 – 5.0 GPa) produces a change in frequency

errors of the higher modes by approximately 4 %, while a limited influence on the first frequency is observed (Fig. 26). It is also worth noting that only a limited influence of the Poisson’s coefficient variation is observed for all the investigated cases. Finally, Figs. 24–26 show lower variability of the MAC indexes against the variability of the material parameters compared to that observed for the frequency errors. It may indicate that MAC indexes are most related to the bridge geometry and boundary conditions rather than material parameters.

### 6. Statistical inference procedure

In this section, a more advanced approach for determining the material properties of the viaduct model is presented, where multi-objective optimisation is employed to obtain accurate fitting with the experimental results. The model parameters reported in Table 11 are assumed as free variables. Two target functions are employed: the absolute error of frequencies and the MAC indexes using different gradient-free and space-partitioning methods. The multi-modal nature of the problem and the number of free variables may require a high number of iterations and considerable computation time to achieve convergence [46] due to the size of the numerical bridge model. Moreover, gradient-free algorithms may not converge or converge to local optimal

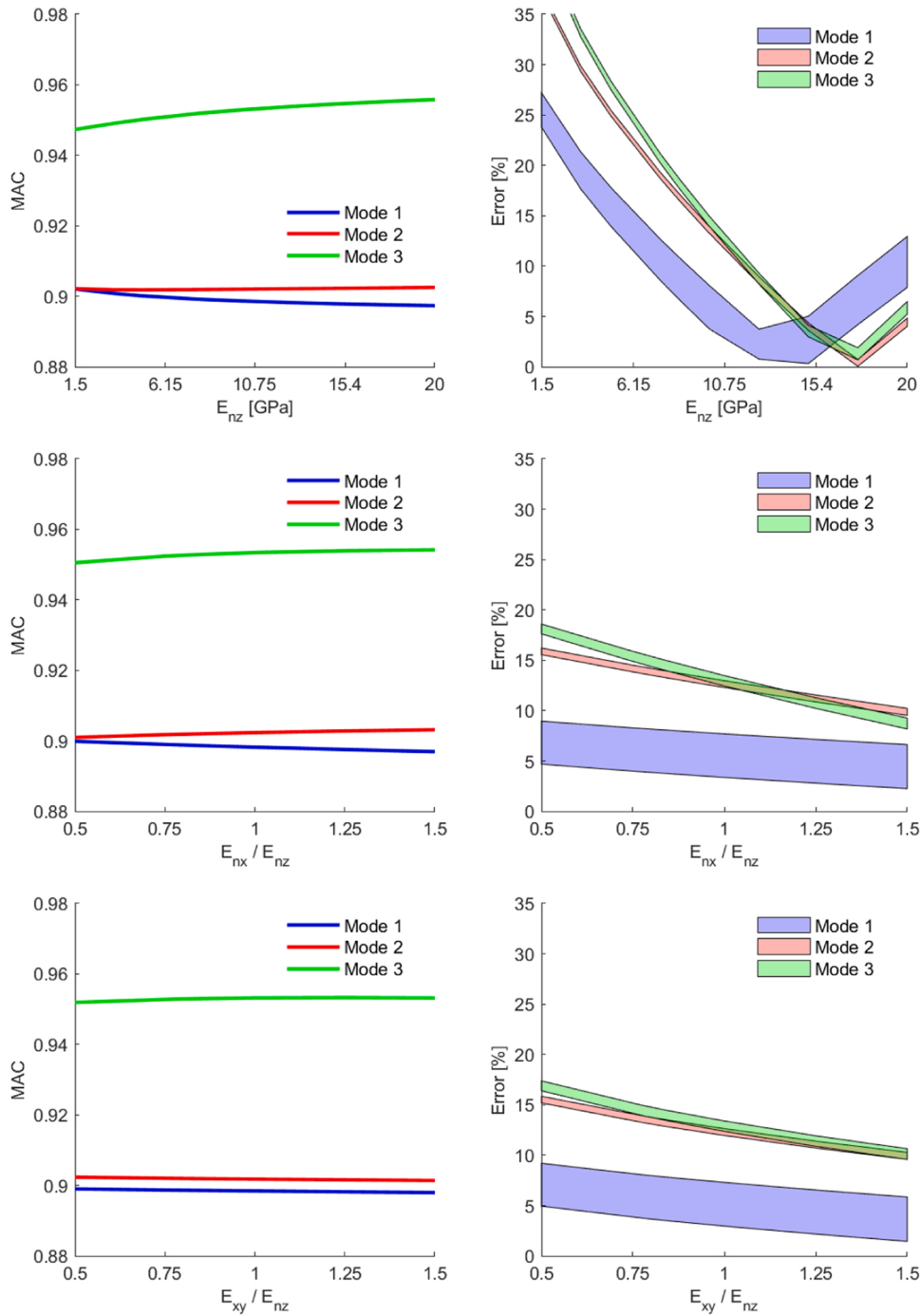


Fig. 24. Model sensitivity to masonry parameters.

solutions. Thus, approaches based on statistical inference can be used to increase the efficiency of the calibration procedure. In this research, a metaheuristic model, also referred to as surrogate model [47,48], has been developed via a stochastic Bayesian algorithm with randomization and exploration of the global space of the material parameters [49]. The surrogate model is used as an adequate replacement of the finite element model of the bridge within an optimisation procedure to establish an optimal set of model material parameters.

### 6.1. The metaheuristic model

Following a metaheuristic modelling approach, the 3D FEM model of the bridge is replaced with the 6-vector 8-variable function as defined in

Eq. (9).

$$\mathbf{f}(\mathbf{X}) = [\Phi_1^T, \Phi_2^T, \Phi_3^T, \omega_1, \omega_2, \omega_3] \quad (9)$$

where:

$\mathbf{X} = [x_1, x_2, \dots, x_8]$  is the vector containing the unknown mechanical parameters;

$\omega_1, \omega_2, \omega_3$  are the first three natural frequencies;

$\Phi_i^T = [\phi_i^1, \phi_i^2, \dots, \phi_i^7]$  ( $i=1,2,3$ ) are the modal shapes associated with the first three modes measured at the seven points monitored by the accelerometers.

The Kriging method is used to represent the numerical model results in Eq. (9). This method has been successfully applied in the literature



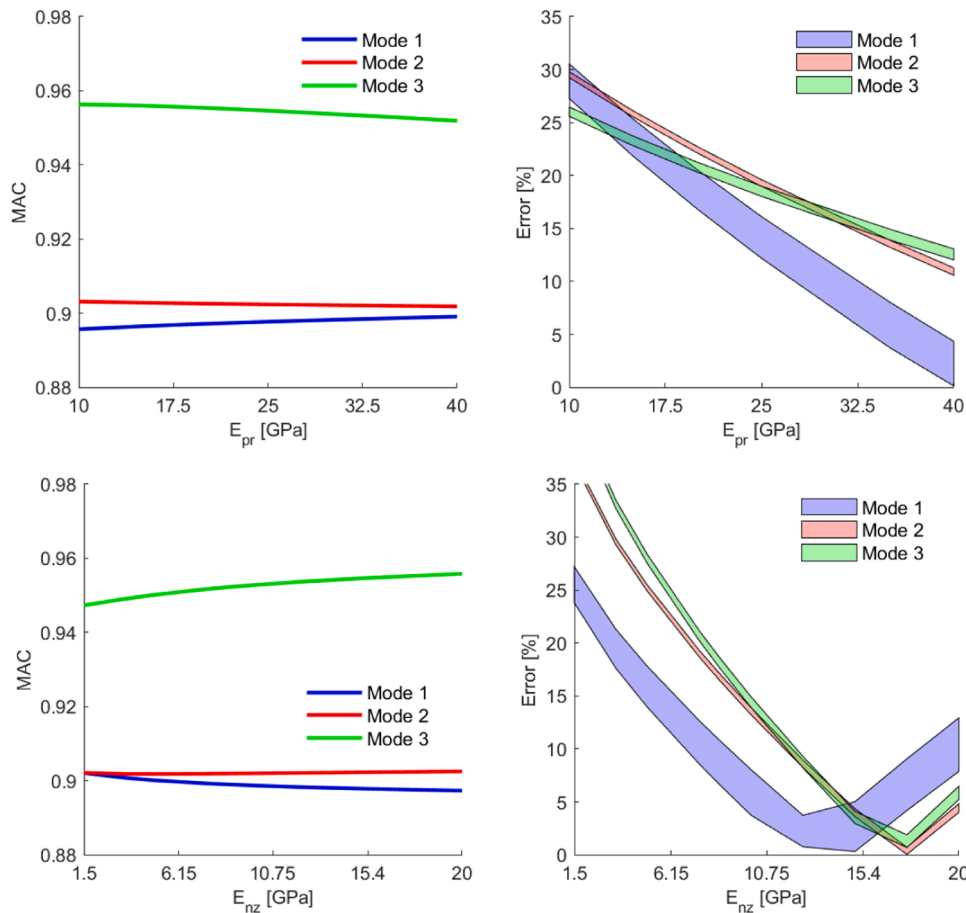


Fig. 25. Sensitivity analyses on piers' infill material.

[48] to solve different problems, including structural robustness design [50]. It approximates each component  $f_p(\mathbf{X})(p = 1, \dots, 24)$  of the function  $\mathbf{f}(\mathbf{X})$  in Eq. (9) as a stochastic process  $\mathcal{M}(\mathbf{X})$ :

$$f_p(\mathbf{X}) \approx \mathcal{M}(\mathbf{X}) = \mathcal{S}_p(\mathbf{X}) + \mathcal{Z}(\mathbf{X}) \quad (10)$$

where  $\mathcal{S}_p(\mathbf{X})$  represents a polynomial regression function defining the mean of the stochastic process  $\mathcal{M}$ , and  $\mathcal{Z}(\mathbf{X})$  denotes the correlation function, an independent stationary covariance process with zero mean and covariance  $\sigma_G^2$ , representing the difference between regression mean  $\mathcal{S}_p(\mathbf{X}^i)$  and the observed value  $f_p(\mathbf{X}^i)$  at the sampled point  $\mathbf{X}^i$ .

The correlation function is defined by adopting the Gaussian kernel model ( $\mathcal{R}$ ) in Eq. (11), where  $d_h$  ( $k = 1, 2, \dots, 8$ ) represents the absolute distance between the sampled points  $\mathbf{X}^i$  and  $\mathbf{X}^j$ ,  $\theta_h$  denotes the hyperparameters defining the regression function. The Gaussian kernel model is adopted due to the nature of the problem, where a smooth transition is expected within the model domain [51].

$$\mathcal{R}(\mathbf{X}^i, \mathbf{X}^j) = \prod_{h=1}^{m=8} \exp(-\theta_h \cdot d_h^2) \quad (11)$$

Combining Eqs. (10) and (11), the Kriging model predictor can be expressed as in Eq. (12), where  $\mathbf{X}^*_{\{1 \times 8\}}$  stands for the predicted points, while  $\widehat{\mathbf{X}}_{\{N \times 8\}}$  denotes points utilised in the creation of the Kriging model.

$$\mathcal{M}(\mathbf{X}^*_{\{1 \times 8\}}) = \mathcal{S}_p(\mathbf{X}^*_{\{1 \times 8\}}) + \mathcal{R}(\mathbf{X}^*_{\{1 \times 8\}}, \widehat{\mathbf{X}}_{\{N \times 8\}})^T \mathcal{R}(\widehat{\mathbf{X}}_{\{N \times 8\}}, \widehat{\mathbf{X}}_{\{N \times 8\}})^{-1} (f_p(\widehat{\mathbf{X}}_{\{N \times 8\}}) - \mathcal{S}_p(\widehat{\mathbf{X}}_{\{N \times 8\}})) \quad (12)$$

Eq. (12) depends on the hyperparameters associated with both correlation and regression functions for each real-valued function of the model, which are obtained by maximising the log-likelihood of the sampled points [48], as in Eq. (13).

$$\mathcal{J} = -\frac{(f_p - \mathcal{S}_p) \cdot \mathcal{R}^{-1} \cdot (f_p - \mathcal{S}_p)}{2 \cdot \sigma_G^2} - \frac{1}{2} \ln(|\mathcal{R}|) - \frac{N}{2} (\ln(\sigma_G^2) + \ln(2\pi)) \quad (13)$$

where  $|\mathcal{R}|$  is the determinant of the correlation matrix and  $N$  is the number of sampled data points, used to define the metamodel.

Eq. (13) represents the objective function of the global multi-modal optimisation problem, used to evaluate the values of the hyperparameters corresponding to its minimum. This optimisation problem is solved using the genetic algorithm approach implemented in MATLAB [52] employing 150 initial population size and a stopping condition based on a maximum of 800 generations and a function tolerance of  $10^{-10}$ .

The initial sample set considered for constructing the Kriging model comprises 6561 observations, corresponding to a hypercube of the 8th order, with each side consisting of 3 points located at the ends and at the middle of the parameter domain. Individual values for each variable are presented in Table 12. This model is used in the optimisation algorithms

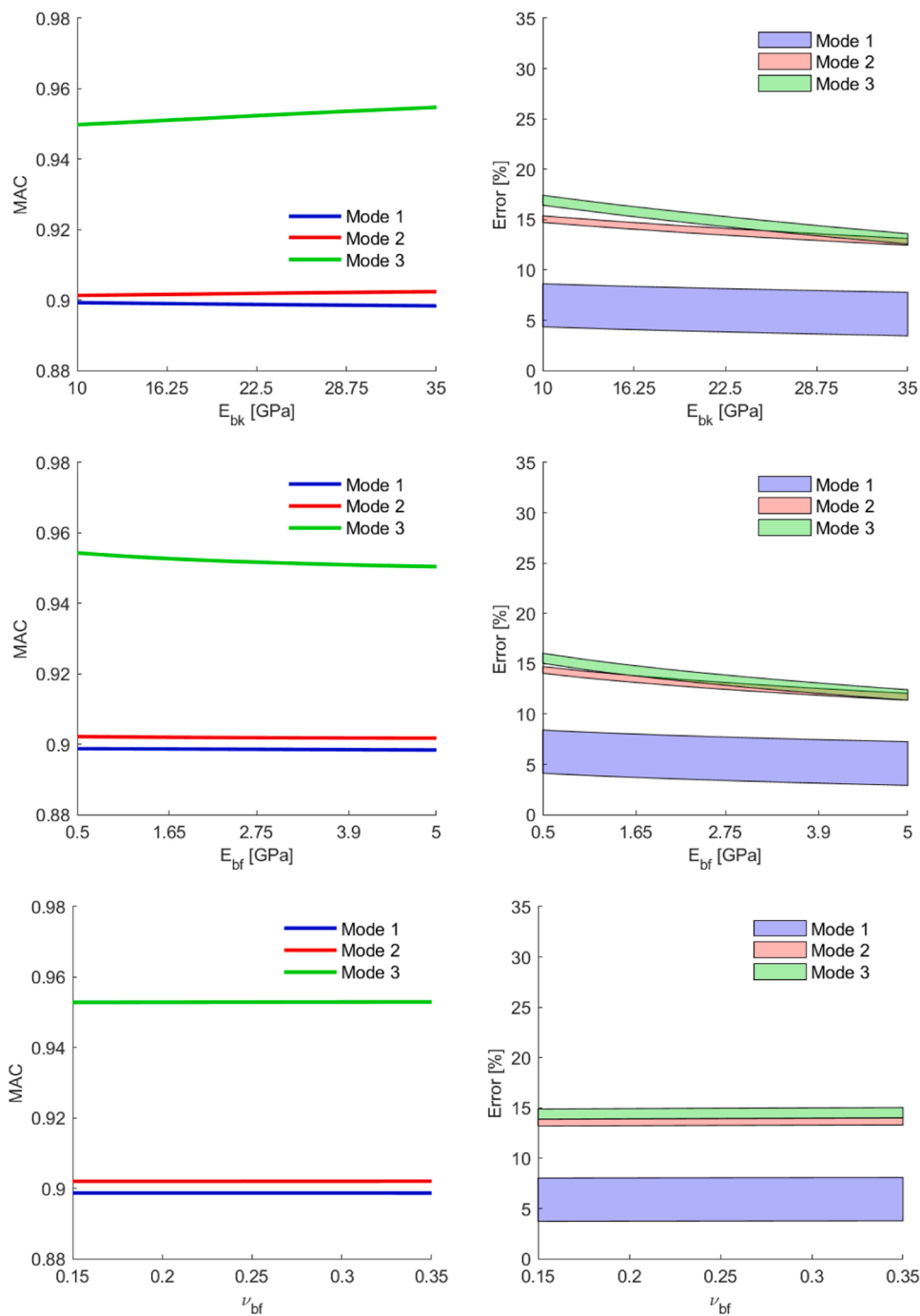


Fig. 26. Sensitivity analyses on backing/backfill parameters.

Table 12  
Kriging sample options.

Sample set	Masonry			Pier Infill		Backfill/Backing		
	$E_{nz}$ (GPa)	$E_{nx}/E_{nz}$ (-)	$E_{xz}/E_{nz}$ (-)	$E_{pr}$ (GPa)	$\nu_{pr}$ (-)	$E_{bk}$ (GPa)	$E_{bf}$ (GPa)	$\nu_{bf} = \nu_{bk}$ (-)
Initial	1.5	0.5	0.5	10	0.15	10	0.5	0.15
	10	1.0	1.0	20	0.25	20	2.5	0.25
	20	1.5	1.5	40	0.35	35	5.0	0.35
Validation	2.5	0.75	0.75	12.5	0.2	15	1.5	0.2
	5			15				
	7.5			17.5				
	12.5	1.25	1.25	25	0.3	27.5	3.5	0.3
	15			27.5				
	17.5			30				

described in Section 6.2 to replace the numerical model.

The model predictions are compared against a validation set consisting of 2304 elements (Table 12), where higher refinement is selected for variables indicating a more complex behaviour according to Section 5.4. According to [50], the overall accuracy of the prediction models is measured by the mean absolute relative error (MARE):

$$MARE = \frac{\sum_{k=1}^N |v_k^{pred} - v_k^{sample}|}{N \cdot (\max(v^{sample}) - \min(v^{sample}))} \quad (14)$$

where  $v_k^{pred}$  represents the value of prediction for the  $k$ -th sample point in the validation set  $\mathbf{V}^{sample}$  consisting of  $N$  individual observations.

Fig. 27 shows the comparison between the metamodel predictions (3D surfaces), the sample points used to build it (black points), and the points used for validation (red points) considering some of the material parameters included as free variables in the optimisation problem.

The Kriging model predictions resulted within acceptable error margins for both MAC values (maximal error for mode one – 2.1 %) and mode frequencies (maximal error for mode three – 1.4 %). Considering the small errors, further optimisation of the hyper-parameters is not required, as it is not expected to substantially improve the achieved model accuracy.

### 6.2. The optimisation problem

The developed surrogate model of the analysed viaduct is employed for the solution of a multi-objective optimisation problem to evaluate the material parameters that correspond to the best fit with the experimental results in terms of mode shapes (measured by the MAC indexes) and frequencies (measured by percentage errors). The consideration of the first three experimental modes of vibrations (Section 5) leads to a total of six objectives. A local space defined by the admissible domain of the free variables, ranging from the lower to the upper bounds of material parameters in Table 11, is assumed. The solution is achieved when all the optimisation criteria are within the allowable range, i.e. the MAC indexes are above 0.9, and the numerical frequencies are within the range of the experimental values indicated in Table 10. The exponential “bump” function ( $\mathcal{M}_k^e$ ) in Eq. (15) is considered for the six objectives of the optimisation problem.

$$\mathcal{M}_k^e = 1 - \exp\left(-\left(\frac{\mathcal{M}_k(\mathbf{X}) - c_k}{D_k}\right)^4\right) \quad (15)$$

where,  $\mathbf{X}$  represents variable input parameters,  $\mathcal{M}_k(\mathbf{X})$  represents  $k$ -th predictor function defined in Eq. (12),  $c_k = \frac{u_k + \ell_k}{2}$  indicates distribution centre,  $D_k = u_k - \ell_k$  denotes the size of the “flat region”, and  $u_k, \ell_k$  stand for upper and lower bound values of the  $k$ -th free variable. This function,

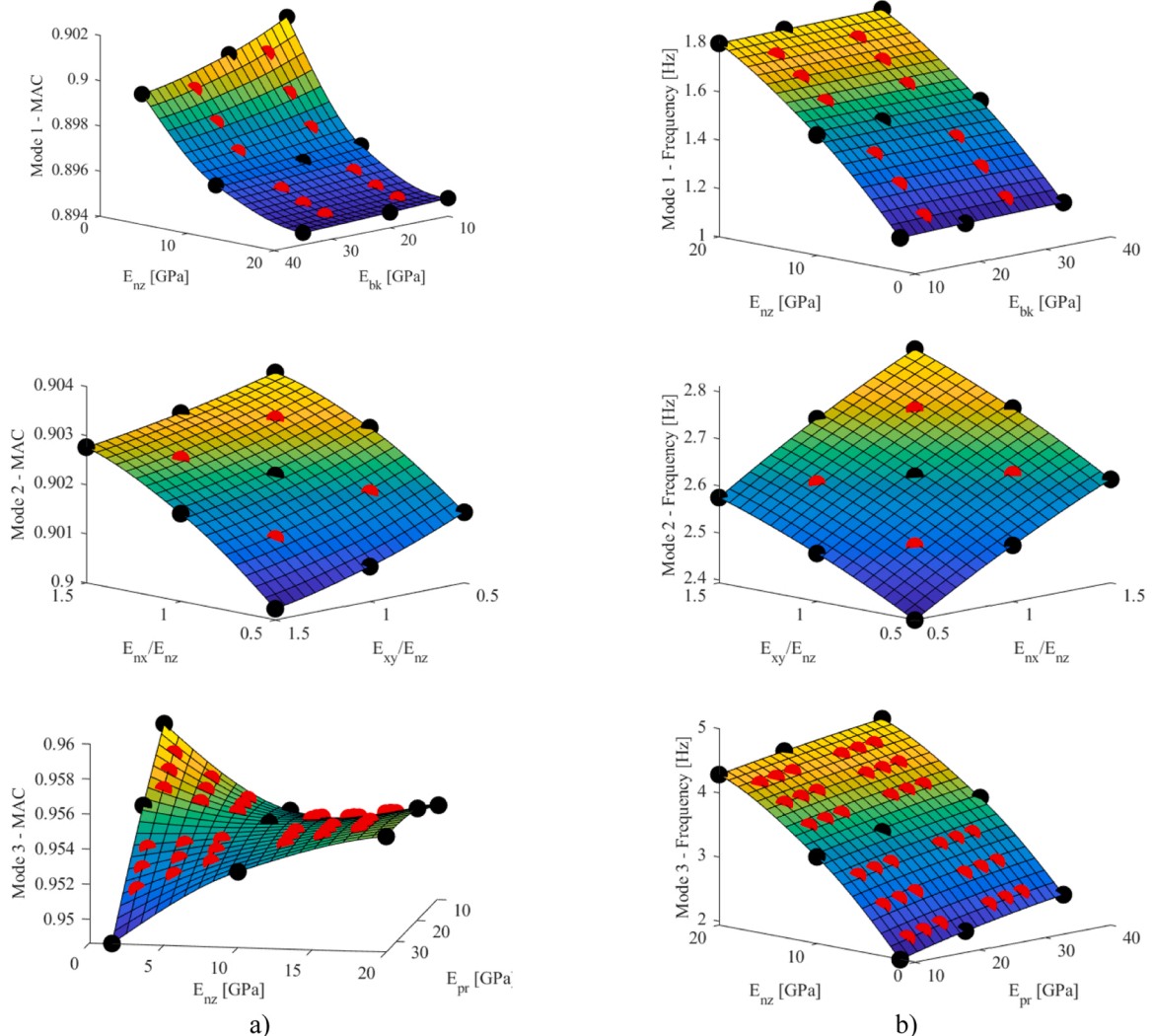


Fig. 27. 2D slices through the parameter domain: a) MAC indexes; b) frequencies.



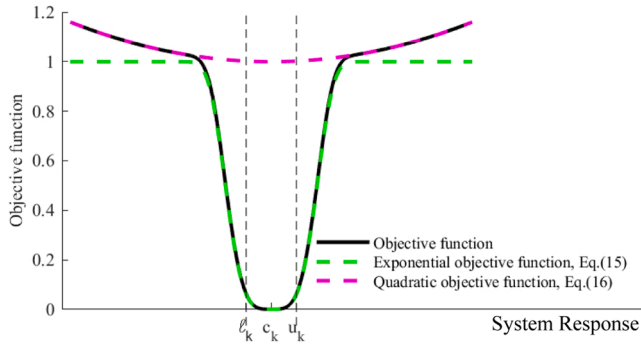


Fig. 28. Objective function.

which is represented with a green dashed line in Fig. 28, can result in non-optimal solutions due to the near zero gradient outside of the acceptable bounds. This can be addressed by considering an additional quadratic function  $\mathcal{H}_k^q$  given by Eq. 16 (magenta curve in Fig. 28) that provides additional scaling to the objective function values away from the optimal range. The constant 0.004 in Eq. (16) is chosen so that the additional quadratic term contribution does not affect the solution within the optimal range. The resultant objective function ( $\mathcal{H}_k$ ) is described as a sum of the exponential ( $\mathcal{H}_k^e$ ) and quadratic ( $\mathcal{H}_k^q$ ) terms and it is shown by the continuous black line in Fig. 28.

$$c_k = \frac{u_k^b + \ell_k^b}{2} \quad (16)$$

Finally, the optimisation problem is formulated as the minimisation of the functions  $\mathcal{H}_k$  in Eq. (17) with  $k = 1, 2, \dots, 6$  associated with the MAC indexes and the frequency errors, where  $\mathbf{X}^l = [x_1^l, x_2^l, \dots, x_8^l]$  and  $\mathbf{X}^u = [x_1^u, x_2^u, \dots, x_8^u]$  are the feasibility constraints in the parameter space  $\mathbf{X} = [x_1, x_2, \dots, x_8]$ .

$$\begin{aligned} &\min(\mathcal{H}_1(\mathbf{X}), \mathcal{H}_2(\mathbf{X}), \dots, \mathcal{H}_6(\mathbf{X})) \\ &\text{s.t. : } x_i^l \leq x_i \leq x_i^u (i = 1, 2, \dots, 8) \end{aligned} \quad (17)$$

The problem in Eq. (17) is solved by evaluating the full 6-dimension Pareto front and selecting for comparison the solution that is closest to the origin of the Pareto front space. Some projections of the Pareto front in the 2D or 3D space are shown in Fig. 29. A variant of the elitist genetic algorithm NSGA-II [53], as implemented in MATLAB [52], is employed to evaluate the Pareto front. Over 24,000 individual calls (120 generation with population of 200) to the numerical model  $\mathcal{H}(\mathbf{X})$  were required to evaluate the Pareto front, which is associated with low efficiency.

An improved optimisation strategy has been introduced to further improve the computational performance. Considering that all objectives are error based, it is possible to implement linear scalarisation of the problem without substantial loss in accuracy [54,55]. A new objective function  $F(\mathbf{X}, \mathbf{P})$  can be established as below:

$$\mathcal{F}(\mathbf{X}, \mathbf{P}) = \frac{\sum_{k=1}^m (\mathcal{H}_k(\mathbf{X}) \cdot p_k)}{\sum_{k=1}^m (p_k)} \quad (18)$$

where,  $\mathbf{P} = [p_1, p_2, \dots, p_6]$  is a set of scalar parameters modifying the relative weight of each individual objective. The simplest scenario is the assumption that all  $p_k$  are equal, meaning that all objectives are of equal importance. Alternatively, specific values can attribute preference for some objectives to be satisfied first (e.g. selecting improved MAC values over mode frequencies or vice versa). The new optimisation problem with the corresponding constraints can be established as follows:

$$\begin{aligned} &\min(\mathcal{F}(\mathbf{X}, \mathbf{P})) \\ &\text{s.t. : } x_i^l \leq x_i \leq x_i^u (i = 1, 2, \dots, 8) \\ &1 \leq p_k \leq 100 (k = 1, 2, \dots, 6) \end{aligned} \quad (19)$$

where, the  $p_k$  values are bounded from 1 to 100 to ensure that no objective can be removed from the analysis.

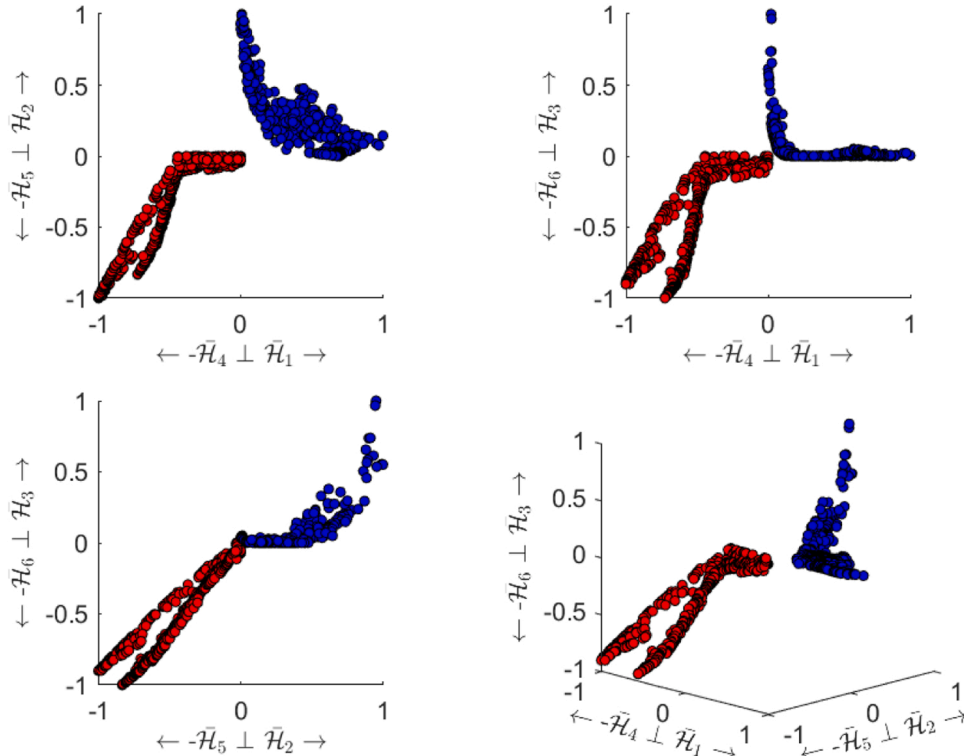


Fig. 29. Six-dimensional normalised Pareto front projections on a three-dimensional space.

The problem in Eq. (19) has been solved assuming the components of the objective ranking vector ( $\mathbf{P}$ ) both as constant set a priori (a) and as additional variables (b). Two separate strategies were used: a gradient based optimisation employing the MATLAB inbuilt function *fmincon* [52] and a Bayesian optimisation with the *Expected Improvement Criterion* [56,57]. Gradient optimisation performed well by using the results obtained in the simplified calibration in Section 5 as the starting points. Due to the lack of analytical expressions for the optimised function derivatives, gradient optimisation required a relatively large number of calls to the surrogate model to achieve convergence: 1016 calls and 126 iterations for option (a) and 3024 calls with 215 iterations for option (b). Bayesian optimisation, which combines space exploration and exploitation in search of the optimal solution [58], was conducted using the Kriging metamodel introduced in Section 6.1. In this context exploitation refers to iterative sampling in the vicinity of prior data points to find the exact location of local minimum, while exploration refers to the samples being taken in the underexplored parts of the design domain. In the first stage of optimisation process, a random sample of 10 points was introduced to create a rough approximation of the response space. At each optimisation step, this approximation was improved including a new point from the previous iteration. It was obtained by maximising the improvement ( $I$ ) of the function  $\mathcal{M}$  given by Eq. (20), after adding an additional sample point  $\mathbf{X}^*$  to the model.

$$I = \max(\min(\mathcal{M}) - \mathcal{M}(\mathbf{X}^*), 0) \tag{20}$$

According to [59] that the expectation of improvement takes the following form:

$$E[I(\mathbf{X}^*)] = (\mathcal{M}_{\min} - \widehat{\mathcal{M}}(\mathbf{X}^*)) \cdot \Psi\left(\frac{\mathcal{M}_{\min} - \widehat{\mathcal{M}}(\mathbf{X}^*)}{\varphi}\right) + \varphi \cdot \Phi\left(\frac{\mathcal{M}_{\min} - \widehat{\mathcal{M}}(\mathbf{X}^*)}{\varphi}\right) \tag{21}$$

where  $\Psi(\cdot)$  and  $\Phi(\cdot)$  denote the cumulative distribution function and the probability density function of the normal distribution,  $\widehat{\mathcal{M}}(\mathbf{X}^*)$  represents a predicted value at an unsampled point  $\mathbf{X}^* = [x_1^*, x_2^*, \dots, x_8^*]^T$  and  $\varphi$  denotes the Kriging surrogate model parameter associated with the confidence level behind the predicted response at the unsampled location:

$$\left\{ \begin{aligned} \varphi(\mathbf{X}^*_{\{1 \times 8\}}) &= \sigma_G^2 \cdot \left( \mathbf{1} + \mathbf{u}^T \cdot (\mathbf{F}^T \cdot \mathcal{R}^{-1} \cdot \mathbf{F})^{-1} \cdot \mathbf{u} - \mathbf{r}^T \cdot \mathcal{R}^{-1} \cdot \mathbf{r} \right) \\ \mathbf{u} &= \mathbf{F}^T \cdot \mathcal{R}^{-1} \cdot \mathbf{r} - \mathbf{f} \\ \mathbf{F} &= \mathcal{S}_p(\widehat{\mathbf{X}}_{\{N \times 8\}}) \\ \mathbf{f} &= \mathcal{S}_p(\mathbf{X}^*_{\{1 \times 8\}}) \\ \mathcal{R} &= \text{corr}(\widehat{\mathbf{X}}_{\{N \times 8\}}, \widehat{\mathbf{X}}_{\{N \times 8\}}) \\ \mathbf{r} &= \text{corr}(\mathbf{X}^*_{\{1 \times 8\}}, \widehat{\mathbf{X}}_{\{N \times 8\}}) \end{aligned} \right. \tag{22}$$

Bayesian optimisation required 300 iterations to converge to the optimal solution showing higher efficiency for cases (a) and (b) compared to gradient optimisation. It is worth noting that although Bayesian optimization required fewer steps and iterations than gradient optimisation, the optimisation was more computational demanding as the calculations in (20–21) required the solution of a further internal optimisation problem at each iteration to locate the best starting point

**Table 13**  
Optimisation results - variables.

Optimised parameters	Masonry			Pier Infill		Backfill/Backing		
	$E_{nz}$ (GPa)	$E_{nx}/E_{nz}$ (-)	$E_{xz}/E_{nz}$ (-)	$E_{pr}$ (GPa)	$\nu_{pr}$ (-)	$E_{bk}$ (GPa)	$E_{bf}$ (GPa)	$\nu_{bf}=\nu_{bk}$ (-)
Pareto front	16.17	0.64	1.15	33.14	0.34	22.21	4.91	0.29
Gradient (a)	20.00	0.63	1.50	17.66	0.15	25.26	3.77	0.15
Gradient (b)	17.38	0.61	1.47	22.84	0.18	25.12	2.69	0.22
Bayesian (a)	15.00	1.48	0.93	27.71	0.20	25.62	3.38	0.24
Bayesian (b)	14.80	0.98	1.13	31.34	0.26	19.31	3.31	0.19

for the subsequent iteration. Though, if in the optimisation procedure the actual numerical viaduct model were used instead of its surrogate approximation, the greater complexity of the Bayesian algorithm would be offset by the computational cost associated with the multiple solutions of the large 3D FE model.

The results obtained using the alternative optimisation strategies are presented in Table 13, in terms of the evaluated set of material parameters, and in Table 14, in terms of MAC indexes and associated objectives. It is shown that no optimisation algorithm yields a single solution in the parameter space, while all of the objectives are in the required vicinity with only minor discrepancies. This fact can be attributed to the overall complexity of multi-objective functions when aggregated, even if each objective is smooth (Figs. 27 and 28).

Comparing the presented results with results from the simplified calibration reported in Table 10 and Fig. 23, very little changes in the prediction of the mode shapes can be observed, as indicated by the near identical MAC values for all the calibration scenarios. On the other hand, a substantial improvement, compared to the simplified calibration, has been found for the determination of modal frequencies, reducing maximal error from 0 (results within the allowable range) to 4 %. The relative errors for all the considered calibration strategies are presented in Table 15.

The provided results indicate that the structure mode shapes are mostly dependent on structural geometry and are only weakly correlated with material properties. Mode frequencies, on the other hand, seem to be strongly correlated with material parameters of the structure, as indicated by the results from the refined optimisation procedure and the sensitivity study presented in Figs. 24–27 (Section 5.4).

## 7. Conclusions

This paper exploits multiple in-situ non-destructive testing techniques for evaluating the mechanical properties of the components of a historic masonry bridge. The results of the tests have been employed to calibrate the elastic properties of an anisotropic continuum macroscale model for masonry and a continuum isotropic model for backfill and inner fill materials by adopting two alternative calibration strategies, characterised by different levels of complexity and accuracy. The first strategy directly considers the NDTs results within a straightforward

**Table 14**  
Optimisation results - objectives.

Optimised results	MAC 1	MAC 2	MAC 3	Mode 1 frequency (Hz)	Mode 2 frequency (Hz)	Mode 3 frequency (Hz)
Pareto front	0.908	0.901	0.951	1.752	2.702	3.998
Gradient (a)	0.896	0.901	0.953	1.672	2.699	4.099
Gradient (b)	0.897	0.901	0.953	1.665	2.691	3.972
Bayesian (a)	0.895	0.903	0.955	1.673	2.708	4.172
Bayesian (b)	0.897	0.902	0.954	1.700	2.695	3.991

**Table 15**  
Relative errors for all calibration strategies.

	Frequency error (%)		
	Mode 1	Mode 2	Mode 3
Simplified calibration (Section 5)	3.76	13.21	13.93
Pareto front	3.09	0.00	0.08
Gradient (a)	0.00	0.00	2.60
Gradient (b)	0.00	0.11	0.00
Bayesian (a)	0.00	0.00	4.42
Bayesian (b)	0.03	0.00	0.00

masonry homogenisation procedure. The second, more sophisticated, strategy determines the model parameters by solving a multi-objective optimisation problem, adopting genetic and statistic inference algorithms. The accuracy of the calibrated model has been evaluated by comparing the numeric mode shapes and frequencies with those obtained experimentally considering the environmental vibrations of the bridge. The model, calibrated by following the simplified strategy, predicted the dynamic properties of the bridge with a satisfactory level of approximation, showing MAC indexes close to 0.9 and an error on the first frequency less than 4 % but errors up to 15 % for the higher order frequencies. On the other hand, the calibration strategy utilising Bayesian optimisation algorithms has almost zeroed the frequency errors for all considered modes, which confirms the accuracy and potential of the proposed strategy for enhanced calibration of existing structures. Finally, the proposed identification methodology can be extended by applying forced vibrations generated by high-speed vehicles, exciting the bridge's higher modes.

#### CRedit authorship contribution statement

**L. Macorini:** Writing – review & editing, Methodology, Investigation, Conceptualization. **B.A. Izzuddin:** Writing – review & editing, Methodology, Investigation, Conceptualization. **S. Grosman:** Writing – review & editing, Writing – original draft, Methodology, Investigation, Conceptualization. **D.V. Oliveira:** Writing – review & editing, Methodology, Investigation, Conceptualization. **P.B. Lourenço:** Writing – review & editing, Methodology, Investigation, Conceptualization. **B. Panto:** Writing – review & editing, Writing – original draft, Methodology, Investigation, Conceptualization. **J. Ortega:** Writing – review & editing, Writing – original draft, Methodology, Investigation, Conceptualization.

#### Declaration of Competing Interest

The authors declare they have no conflicts of interest to declare.

#### Data availability

Data will be made available on request.

#### Acknowledgments

The first author gratefully acknowledges support from the Marie Skłodowska-Curie Individual fellowship under Grant Agreement 846061 (Project Title: Realistic Assessment of Historical Masonry Bridges under Extreme Environmental Actions, “RAMBEA”, <https://cordis.europa.eu/project/id/846061>).

This work was partly financed by FCT/MCTES through national funds (PIDDAC) under the R&D Unit Institute for Sustainability and Innovation in Structural Engineering (ISISE), under reference UIDB / 04029/2020 (doi.org/10.54499/UIDB/04029/2020), and under the Associate Laboratory Advanced Production and Intelligent Systems ARISE under reference LA/P/0112/2020.

The authors gratefully acknowledge the support from the Portuguese

Road and Railway Infrastructure Manager Company (Infraestruturas de Portugal) and, in particular, from Eng. Hugo Patrício for providing key technical documentation.

#### References

- [1] Z. Orbán, Assessment, reliability and maintenance of masonry arch railway bridges in Europe, in: P. Roca, C. Molins (Eds.), *Arch Bridges IV—Advances in Assessment, Structural Design and Construction*, Barcelona, 2004, pp. 152–161.
- [2] T. Forgács, V. Sarhosis, S. Ádány, Shakedown and dynamic behaviour of masonry arch railway bridges, *Eng. Struct.* 228 (2021) 111474.
- [3] J. George, A. Menon, Analytical fragility curves for displacement-based scour assessment of masonry arch bridges, in: *Structures*, Elsevier, 2022, pp. 172–185.
- [4] E. Tubaldi, L. Macorini, B.A. Izzuddin, Three-dimensional mesoscale modelling of multi-span masonry arch bridges subjected to scour, *Eng. Struct.* 165 (2018) 486–500.
- [5] Melbourne, C., McKibbins, L.D., Sawar, N., & Gaillard, C.S. (2006). *Masonry arch bridges: condition appraisal and remedial treatment*. Ciria, London.
- [6] B. Conde, L.F. Ramos, D.V. Oliveira, B. Riveiro, M. Solla, Structural assessment of masonry arch bridges by combination of non-destructive testing techniques and three-dimensional numerical modelling: application to Vilanova bridge, *Eng. Struct.* 148 (2017) 621–638.
- [7] V.N. Moreira, J.C. Matos, D.V. Oliveira, Probabilistic-based assessment of a masonry arch bridge considering inferential procedures, *Eng. Struct.* 134 (2017) 61–73.
- [8] E. Tubaldi, L. Macorini, B.A. Izzuddin, C. Manes, F. Laio, A framework for probabilistic assessment of clear-water scour around bridge piers, *Struct. Saf.* 69 (2017) 11–22.
- [9] F. da Porto, G. Tecchio, P. Zampieri, C. Modena, A. Prota, Simplified seismic assessment of railway masonry arch bridges by limit analysis, *Struct. Infrastruct. Eng.* 12 (5) (2016) 567–591.
- [10] B. Pantò, C. Chisari, L. Macorini, B.A. Izzuddin, A hybrid macro-modelling strategy with multi-objective calibration for accurate simulation of multi-ring masonry arches and bridges, *Comp. Struct.* 265 (2022) 106769.
- [11] B. Pantò, S. Grosman, L. Macorini, B.A. Izzuddin, A macro-modelling continuum approach with embedded discontinuities for the assessment of masonry arch bridges under earthquake loading, *Eng. Struct.* 269 (2022) 114722.
- [12] V. Sarhosis, T. Forgács, J.V. Lemos, A discrete approach for modelling backfill material in masonry arch bridges, *Comput. Struct.* 224 (2019) 106108.
- [13] B. Pulatsu, E. Erdogmus, P.B. Lourenço, Comparison of in-plane and out-of-plane failure modes of masonry arch bridges using discontinuum analysis, *Eng. Struct.* 178 (2019) 24–36.
- [14] S. Caddemi, I. Calliò, F. Cannizzaro, D. D'Urso, B. Pantò, D. Rapicavoli, G. Occhipinti, 3D discrete macro-modelling approach for masonry arch bridges, *IABSE Symp.* (2019) 27–29.
- [15] C. Chisari, L. Macorini, B.A. Izzuddin, Multiscale model calibration by inverse analysis for nonlinear simulation of masonry structures under earthquake loading, *Int. J. Multiscale Comput. Eng.* 18 (2) (2020).
- [16] A. Arede, C. Costa, A.T. Gomes, J.E. Menezes, R. Silva, M. Morais, R. Goncalves, Experimental characterization of the mechanical behaviour of components and materials of stone masonry railway bridges, *Constr. Build. Mater.* 153 (2017) 663–681.
- [17] J. Ortega, M. Stepinac, L. Lulić, M.N. García, S. Saloustros, C. Aranha, F. Greco, Correlation between sonic pulse velocity and flat-jack tests for the estimation of the elastic properties of unreinforced brick masonry: case studies from Croatia, *Case Stud. Constr. Mater.* 19 (2023) e02467.
- [18] Z. Orbán, M. Gutermann, Assessment of masonry arch railway bridges using non-destructive in-situ testing methods, *Eng. Struct.* 31 (10) (2009) 2287–2298.
- [19] L.J. Sánchez-Aparicio, Á. Bautista-De Castro, B. Conde, P. Carrasco, L.F. Ramos, Non-destructive means and methods for structural diagnosis of masonry arch bridges, *Autom. Constr.* 104 (2019) 360–382.
- [20] P. Borlenghi, A. Saisi, C. Gentile, ND testing and establishing models of a multi-span masonry arch bridge, *J. Civ. Struct. Health Monit.* (2023) 1–17.
- [21] Séjourné, Paul. *Grandes voûtes*. Vol. 5. Impr. Vve Tardy-Pigelet et fils, 1915.
- [22] SVS, ARTEMIS Extractor Pro User Manual, Release 3.5, SVS, Structural Vibration Solutions, Aalborg, Denmark, 2006.
- [23] Miroslav Pastor, Michal Binda, Tomáš. Harčarik, Modal Assurance Criterion, *Procedia Eng.* 48 (2012) 543–548.
- [24] L. Binda, A. Saisi, C. Tiraboschi, Investigation procedures for the diagnosis of historic masonries, *Constr. Build. Mater.* 14 (4) (2000) 199–233.
- [25] L. Qixian, J.H. Bungey, Using compression wave ultrasonic transducers to measure the velocity of surface waves and hence determine dynamic modulus of elasticity for concrete, *Constr. Build. Mater.* 10 (4) (1996) 237–242.
- [26] T.M. Ferreira, N. Mendes, R. Silva, P.B. Lourenço, Non-destructive testing, assessment, and strengthening for reducing the seismic vulnerability of masonry structures, *Mason. Constr. Act. Seism. Reg.* (2021) 123–146.
- [27] L.F. Miranda, J. Rio, J.M. Guedes, A. Costa, Sonic Impact Method—A new technique for characterization of stone masonry walls, *Constr. Build. Mater.* 36 (2012) 27–35.
- [28] EN 12504-4 (2004) Testing concrete— Part 4: Determination of ultrasonic pulse velocity, European Committee for Standardization.
- [29] M. Everett, *Near-Surface Applied Geophysics*, Cambridge University Press, USA, 2013.



- [30] Vasconcelos G. (2005) Experimental investigations on the mechanics of stone masonry: Characterization of granites and behavior of ancient masonry shear walls, PhD Thesis, University of Minho.
- [31] A. Sadri, Application of impact-echo technique in diagnoses and repair of stone masonry structures, *NDTE Int.* 36 (2003) 195–202.
- [32] V. Malhotra, N. Carino, Handbook on Non-destructive Testing of Concrete, CRC Press LLC, ASTM International, West Conshohocken, PA, USA, 2004.
- [33] A. Nagy, Determination of E-Modulus of Young Concrete with Non-destructive Method, *J. Mater. Civ. Eng.* 9 (1) (1997) 15–20.
- [34] Y. Zhou, J. Gao, Z. Sun, W. Qu, A fundamental study on compressive strength, static and dynamic elastic moduli of young concrete, *Constr. Build. Mater.* 98 (2015) 137–145.
- [35] N. Makoond, L. Pelà, C. Molins, Dynamic elastic properties of brick masonry constituents, *Constr. Build. Mater.* 199 (2019) 756–770.
- [36] A. D'Ambrisi, V. Mariani, M. Mezzi, Seismic assessment of a historic masonry tower with nonlinear static and dynamic analyses tuned on ambient vibration tests, *Eng. Struct.* 36 (2012) 210–219.
- [37] M. Ripepe, M. Coli, G. Lacanna, E. Marchetti, M.T. Cristofaro, M. De Stefano, V. Mariani, Dynamic response of the Giotto's Bell-Tower, Firenze, IT, *Eng. Geol. Soc. Territ.* 8 (2014) 323–327.
- [38] B.A. Izzuddin, Nonlinear Dynamic Analysis of Framed Structures, Ph.D. Thesis, Imperial College, University of London, London, 1991. Available at: [spiral:8443/handle/10044/1/8080](https://hdl.handle.net/10044/1/8080).
- [39] S. Grosman, L. Macorini, B.A. Izzuddin, Parametric nonlinear modelling of 3D masonry arch bridges (Available at:), *Adv. Eng. Softw.* 185 (2023) 103514, <https://doi.org/10.1016/j.advengsoft.2023.103514>.
- [40] R. McNeel, Associates, Rhinoceros 3D, Version 6.0, Robert McNeel Assoc, Seattle, WA, 2010.
- [41] E. Minga, L. Macorini, B. Izzuddin, Enhanced mesoscale partitioned modelling of heterogeneous masonry structures, *Int. J. Numer. Methods Eng.* 113 (13) (2018) 1950–1971.
- [42] G.A. Jokhio, B.A. Izzuddin, A dual super-element domain decomposition approach for parallel nonlinear finite element analysis, *Int. J. Comput. Methods Eng. Sci. Mech.* 16 (3) (2015) 188–212.
- [43] L. Macorini, B.A. Izzuddin, A nonlinear interface element for 3D mesoscale analysis of brick-masonry structures. *Int. J. Numer. Methods Eng.* 85 (12) (2011) 1584–1608.
- [44] B. Pantò, L. Macorini, B.A. Izzuddin, A two-level macroscale continuum description with embedded discontinuities for nonlinear analysis of brick/block masonry, *Comput. Mech.* 69 (3) (2022) 865–890.
- [45] B. Ghiassi, G. Milani, Numerical Modeling of Masonry and Historical Structures: from Theory to Application, Woodhead Publishing, 2019.
- [46] V. Ojha, B. Pantò, G. Nicosia, Adaptive search space decomposition method for pre- and post-buckling analyses of space truss structures, *Eng. Appl. Artif. Intell.* 117 (2023) 105593.
- [47] A. Forrester, et al., Engineering Design Via Surrogate Modelling: A Practical Guide, John Wiley & Sons, 2008.
- [48] J.P. Kleijnen, Kriging metamodeling in simulation: a review, *Eur. J. Oper. Res.* 192 (3) (2009) 707–716.
- [49] A.H. Gandomi, X.S. Yang, S. Talatahari, A.H. Alavi, Metaheuristic Applications in Structures and Infrastructures, Newnes, 2013.
- [50] S. Grosman, Critical local damage scenarios for robustness assessment of irregular structures (Doctoral dissertation), Imperial College, London, 2019, 10.25560/76498.
- [51] L. Laurent, R. Le Riche, B. Soulier, P.A. Boucard, An overview of gradient-enhanced metamodels with applications, *Arch. Comput. Methods Eng.* 26 (1) (2019) 61–106.
- [52] The MathWorks Inc (2012) MATLAB and Statistics Toolbox Release 2012b. Natick, Massachusetts, United States.
- [53] K. Deb, A. Pratap, S. Agarwal, T.A.M.T. Meyarivan, A fast and elitist multiobjective genetic algorithm: NSGA-II, *IEEE Trans. Evolut. Comput.* 6 (2) (2002) 182–197.
- [54] G.G. Wang, S. Shan, An efficient pareto set identification approach for multi-objective optimization on black-box functions, *Int. Des. Eng. Tech. Conf. Comput. Inf. Eng. Conf.* 46946 (2004) 279–291.
- [55] A. Ghane-Kanafi, E. Khorram, A new scalarization method for finding the efficient frontier in non-convex multi-objective problems, *Appl. Math. Model.* 39 (23-24) (2015) 7483–7498.
- [56] A.I. Forrester, A.J. Keane, Recent advances in surrogate-based optimization, *Prog. Aerosp. Sci.* 45 (1-3) (2009) 50–79.
- [57] A. Forrester, A. Sobester, A. Keane, Engineering Design Via Surrogate Modelling: A Practical Guide, John Wiley & Sons, 2008.
- [58] A. Sobester, S.J. Leary, A.J. Keane, On the design of optimization strategies based on global response surface approximation models, *J. Glob. Optim.* 33 (2005), 31–59.1.
- [59] V. Nguyen, S. Gupta, S. Rana, C. Li, S. Venkatesh, Regret for expected improvement over the best-observed value and stopping condition, in: Asian conference on machine learning, PMLR, 2017, pp. 279–294.